Monthly Notices of the ROYAL ASTRONOMICAL SOCIETY

MNRAS **504,** 4428–4444 (2021) doi:10.1093/mnras/stab1163
Advance Access publication 2021 April 23

Isocyanic acid (HNCO) in the hot molecular core G331.512-0.103: observations and chemical modelling

Carla M. Canelo ,[1]★ Leonardo Bronfman,[2]★ Edgar Mendoza,[1,3]★ Nicolas Duronea,[4] Manuel Merello ,[2] Miguel Carvajal ,[5,6] Amâncio C. S. Friaça[1] and Jacques Lepine[1]

[1]*Departamento de Astronomia, Instituto de Astronomia, Geofísica e Ciências Atmosféricas, Universidade de São Paulo, São Paulo, 05508-090, Brazil*
[2]*Departamento de Astronomía, Universidad de Chile, Casilla 36-D, Santiago de Chile, Chile*
[3]*Observatório do Valongo, Universidade Federal do Rio de Janeiro, Ladeira Pedro Antônio, 43, Rio de Janeiro, RJ 20.080-090, Brazil*
[4]*Instituto de Astrofísica de La Plata (UNLP - CONICET), La Plata, Argentina*
[5]*Dept. Ciencias Integradas, Facultad de Ciencias Experimentales, Centro de Estudios Avanzados en Física, Matemática y Computación, Unidad Asociada GIFMAN, CSIC-UHU, Universidad de Huelva, Spain*
[6]*Instituto Universitario Carlos I de Física Teórica y Computacional, Universidad de Granada, Spain*

Accepted 2021 April 20. Received 2021 April 20; in original form 2021 January 27

ABSTRACT

Isocyanic acid (HNCO) is a simple molecule with a potential to form prebiotic and complex organic species. Using a spectral survey collected with the *Atacama Pathfinder EXperiment*, in this work we report the detection of 42 transitions of HNCO in the hot molecular core/outflow G331.512-0.103 (hereafter G331). The spectral lines were observed in the frequency interval ∼160–355 GHz. By means of Local Thermodynamic Equilibrium analyses, applying the rotational diagram method, we studied the excitation conditions of HNCO. The excitation temperature and column density are estimated to be T_{ex}= 58.8 ± 2.7 K and $N = (3.7 \pm 0.5) \times 10^{15}$ cm^{-2}, considering beam dilution effects. The derived relative abundance is between $(3.8 \pm 0.5) \times 10^{-9}$ and $(1.4 \pm 0.2) \times 10^{-8}$. In comparison with other hot molecular cores, our column densities and abundances are in agreement. An update of the internal partition functions of the four CHNO isomers: HNCO; cyanic acid, HOCN; fulminic acid, HCNO; and isofulminic acid, HONC is provided. We also used the astrochemical code NAUTILUS to model and discuss HNCO abundances. The simulations could reproduce the abundances with a simple zero-dimensional model at a temperature of 60 K and for a chemical age of $\sim 10^5$ yr, which is larger than the estimated dynamical age for G331. This result could suggest the need for a more robust model and even the revision of chemical reactions associated with HNCO.

Key words: astrochemistry – molecular data – molecular processes – methods: observational – ISM: molecules.

1 INTRODUCTION

The isocyanic acid (HNCO) is the simplest molecule containing four of the six biogenic elements: carbon, hydrogen, oxygen, nitrogen, phosphorus, and sulphur (abbreviated as CHONPS) that are present in all living beings. Although it has only four atoms, HNCO could be precursor of other prebiotic and complex organic molecules (COMs[1]), which are of great astrochemical and astrobiological interest due to their potential to form molecules such as amino acids, sugars, and nucleobases (e.g. Gorai et al. 2020, and references therein). HNCO molecules are included as a peptide bond [-(H)N-C(O)-] between any two single amino acid, such as glycine (Fedoseev et al. 2015). Moreover, recent experiments, simulating interstellar ice chemical processes, have shown that HNCO and CH_4 can form molecules with peptide bonds in solid state under far-ultraviolet (UV) irradiation (Ligterink et al. 2018). The observation of COMs in astrophysical environments, along with the study of their formation and destruction pathways, are important for a better comprehension of the origins of life on Earth and elsewhere.

The potential interest of HNCO in radio astronomy has generated and stimulated debates, specially about its formation and detection. Among the first experimental works, Jones et al. (1950) and Jones & Badger (1950) made experimental investigations of the infrared and microwave spectra of HNCO and HNCS. Hocking, Gerry & Winnewisser (1972, 1975) carried out laboratory measurements to study the HNCO microwave and millimetre spectrum. Concurrently, Snyder & Buhl (1972) reported the results of a survey for HNCO in Galactic molecular sources, concluding about its detection in Sgr B2. HNCO is a near prolate asymmetric top molecule with a linearity barrier at 1899 cm^{-1} (Niedenhoff et al. 1995); its rotational levels undergo a hyperfine splitting caused by the nuclear spin of nitrogen (Lapinov et al. 2007). The rotational levels of HNCO are assigned by the spectroscopic notation for the asymmetric top, such as J_{K_a,K_c}, where J is the rotational angular momentum, and K_a and K_c are the projections of J to the molecule fixed principal a- and c-axes, respectively (Hocking, Gerry & Winnewisser 1974; Niedenhoff et al. 1995; Zinchenko, Henkel & Mao 2000).

★ E-mail: camcanelo@gmail.com (CMC); leo@das.uchile.cl (LB); emendoza@astro.ufrj.br (EM)

[1]As discussed in Herbst & van Dishoeck (2009), the term complex is labelled by astronomers if not by chemist, and makes a reference to interstellar molecules with six or more atoms including the element carbon.

© 2021 The Author(s)
Published by Oxford University Press on behalf of Royal Astronomical Society

Downloaded from https://academic.oup.com/mnras/article/504/3/4428/6247604 by Universidad de Granada - Biblioteca user on 30 June 2021

Churchwell et al. (1986) found that the most likely excitation mechanism of HNCO in Sgr B2 might be radiative rather than collisional, so the molecule can be an optimal tracer of the far-infrared field (at $\lambda \approx 110$ and 330 μm). As a consequence of the energy structure and short lifetimes of the excited K_a ladders of HNCO, its populational diagram can be substantially induced by far-infrared radiation. In a study based on observations of HNCO ($5_{0,5}$–$4_{0,4}$) in massive star-forming regions, Li et al. (2013) found that the HNCO emission show signs of embedded mid-infrared or far-infrared sources, and also a correlation with emission of HC_3N.

As we mentioned previously, the first detection of HNCO in the interstellar medium (ISM) was towards the molecular cloud complex Sgr B2 (Snyder & Buhl 1972). Since then, HNCO has been periodically reported in several astronomical objects, from comets up to external galaxies. Based on sub-mm observations of comets, Biver et al. (2006) carried out a comparative study of molecules such as CH_3OH, H_2CO, HNCO, among others, towards the comets C/1999 T1 (McNaught-Hartley), C/2001 A2 (LINEAR), C/2000 WM1 (LINEAR), and 153P/Ikeya-Zhang. Lis et al. (1997) performed observations of Comet C/1996 B2 (Hyakutake) and reported for the first time the HNCO $16_{0,16}$–$15_{0,15}$ transition, at $\nu \approx 351633.257$ MHz, in a comet. Crovisier (1998) discussed the presence of HNCO in comets Hyakutake and Hale-Bopp; its synthesis could be associated with the OCN^- anion. In the context of planetary atmospheres, based on Herschel/HIFI-PACS and Cassini/CIRS studies of Titan's atmosphere, Dobrijevic et al. (2014) carried out photochemical models to predict the presence of compounds such as NO, HNCO, and N_2O. In low-mass protostellar objects, HNCO was studied along with NH_2CHO in solar-type protostars and protostellar shocks (Mendoza et al. 2014; López-Sepulcre et al. 2015, 2019).

More recently, Hernández-Gómez et al. (2019) observed HNCO towards IRAS 16293-2422 and computed models using the astrochemical code NAUTILUS. Their study included observations from several telescopes including the *Atacama Pathfinder Experiment* (*APEX*). Considering evolved objects, HNCO was observed in the oxygen-rich circumstellar envelope around an intermediate-mass evolved star, OH231.8+4.2, which harbours a bipolar molecular outflow (Velilla Prieto et al. 2015). In the context of high-mass star-forming regions, Zinchenko et al. (2000) surveyed 81 dense high-mass star-forming regions and emission lines of HNCO were detected towards 57 sources, with a tentative detection of $HN^{13}CO$ ($10_{0,10}$–$9_{0,9}$) at $\sim$ 220 GHz in G310.12-0.20. Gorai et al. (2020) carried out a study of HNCO, NH_2CHO and CH_3NCO in the hot molecular core G10.47+0.03, finding that they are chemically linked with each other according to their data analysis results and chemical models. In the same source, Wyrowski, Schilke & Walmsley (1999) had previously reported the first detection of vibrationally excited HNCO, as part of a study that was mainly focused on HC_3N. In Sgr B2 and Orion KL, Turner (1991) analysed several transitions of HNCO in the frequency interval ~87–220 GHz. In extragalactic sources, Nguyen-Q-Rieu et al. (1991) reported the first detection of HNCO in external galaxies. They observed the $4_{0,4}$–$3_{0,3}$, and $6_{0,6}$–$5_{0,5}$ transitions towards NGC 253 using the *IRAM*-30 m observatory. Meier & Turner (2005) observed emission of HNCO towards the nearby spiral galaxy IC 342, finding a correlation with another tracer as CH_3OH. Martín et al. (2006) analysed the physical conditions of HNCO, among other chemical species, using a 2 mm spectral survey towards NGC 253. Martín, Martín-Pintado & Mauersberger (2009) determined HNCO abundances in galaxies, concluding that HNCO is a good tracer to diagnose the evolutionary state of nuclear starburst.

G331 has proven to be very rich source in molecular emission (e.g. Bronfman et al. 2008; Merello et al. 2013b; Mendoza et al. 2018; Duronea et al. 2019; Hervías-Caimapo et al. 2019) and the analysis of HNCO could be an important tool not only to understand the physical properties of the source but also to complement the inventory of Galactic sources where this molecule has been detected. Moreover, the present study could increase the chemical knowledge of the molecular species and their reaction networks present in G331.

In this work, we focus on the identification of HNCO in the hot molecular core G331, which is one of the most luminous and energetic outflows known in the Galaxy. It is located towards the brightest and most massive dust condensation of the star-forming region of G331.5-0.1, placed in the Norma spiral arm at a heliocentric distance of approximately 7.5 kpc (Merello et al. 2013a). The mass of the core is about 40 $M_\odot$ while the mass of each outflow lobe is about 25 $M_\odot$ (Hervías-Caimapo et al. 2019). G331 also presents a momentum of $\sim 2.4 \times 10^3$ $M_\odot$ km s^{-1} and a kinetic energy of $\sim 1.4 \times 10^{48}$ erg (Bronfman et al. 2008). Such values are expected in flows driven by young massive stellar objects with $L_{bol} \sim 1 \times 10^5$ $L_\odot$ (e.g. Bally 2016). Observations in the *ALMA* band 7 receiver revealed a main hydrogen density of the core of $\sim 5 \times 10^6$ cm^{-3} and a temperature around 70 K (Hervías-Caimapo et al. 2019). Moreover, the observed SiO and SO_2 molecular lines also traced a denser region with temperatures up to 200 K, which suggests an expanding shell-like structure.

Another approach to understand the chemical network of HNCO in G331 is to simulate its abundance with an astrochemical model. The evidence of ammonium salts in comet 67P/Churyumov-Gerasimenko can suggest that species like halides and HNCO are in the form of salt, presenting high sublimation temperatures which would not allow their detection in the gas phase and could explain the relatively low interstellar abundances of HNCO (Altwegg et al. 2020). In this sense, the NAUTILUS code (Ruaud, Wakelam & Hersant 2016) considers both gas and grain reactions to perform time-dependent simulations of molecular abundances in hot and cold molecular cores, which can allow an overview of the HNCO chemistry in G331.

The article is divided as following: Section 2 presents the methodology of the observations and data analysis; Section 3 exhibits the detected lines and their physical analysis; these results are also discussed in Section 4 together with the NAUTILUS simulations; and finally, the summary and conclusions of this work are presented in Section 5.

2 METHODOLOGY

The observations have been obtained with the *APEX* telescope[2] (Güsten et al. 2006) using the single point mode towards the coordinates RA:DEC = $16^h12^m10.1^s$, $-51°28'38.1''$. The spectral line setups were collected over various semesters between 2014 and 2019. We have used APEX-1 and APEX-2 receivers of the Swedish Heterodyne Facility Instrument (SHeFI; Vassilev et al. 2008) to observe bands within the intervals 213–275 GHz and 267–378 GHz, respectively. As backend, the eXtended bandwidth Fast Fourier Transform Spectrometer2 has been used. The spectral

[2]This publication is based on data acquired with the *APEX*, over various semesters between 2014 and 2019, under projects IDs C-094.F-9709B-2014, C-097.F-9710A-2016, C-099.F-9702A-2017, C-0102.F-9702B-2018, and C-0104.F-9703B-2019. APEX is a collaboration between the Max-Planck-Institut fur Radioastronomie, the European Southern Observatory, and the Onsala Space Observatory.

Downloaded from https://academic.oup.com/mnras/article/504/3/4428/6247604 by Universidad de Granada - Biblioteca user on 30 June 2021

resolution, corresponding to a velocity resolution, has been obtained between ∼0.15 and 0.25 km s^{-1} for a noise level of ∼ 30 mK. This paper includes results from the last observations conducted with the SEPIA B5 receiver (Belitsky et al. 2018), since various lines of HNCO were discovered within the frequency interval covered by that receiver (159–211 GHz). For further clarity, the resolution of the spectra exhibited in the present work has been degraded to a common value of 1 km s^{-1}. The original intensity, obtained in scale of antenna temperature (T_a), has been converted to the main-beam temperature (T_{mb}) scale using main-beam efficiency values of $\eta_{mb} \approx 0.80$, 0.75, and 0.73 at the frequencies 208, 230, and 352 GHz,[3] respectively, whose Half Power Beam Width values are within ∼17–30 arcsec.

The data reduction and line identification have been carried out using the CLASS/GILDAS[4] and CASSIS[5] softwares. Lines have been analysed using Spectroscopic databases such as the NIST[6] Recommended Rest Frequencies for Observed Interstellar Molecular Microwave Transitions (Lovas 2004), CDMS[7] (Endres et al. 2016), JPL[8] (Pickett et al. 1998) and Splatalogue.[9] The radiative analyses have been carried out assuming Local Thermodynamic Equilibrium (LTE), excitation temperatures, and column densities were estimated from rotational diagrams (Goldsmith & Langer 1999). The rotational diagrams were constructed using CASSIS, which requires a given calibration uncertainty to compute rotational temperatures and column densities with their respective errors. A calibration uncertainty of 30 per cent (Dumke & Mac-Auliffe 2010) was considered in this work. Descriptions on the methodology and data analysis have been presented in previous works (e.g. Mendoza et al. 2018; Duronea et al. 2019).

3 RESULTS

In general, the spectral lines of HNCO have been identified over the 3σ level. Lines with ladders $K_a = 0$, 1, and 2 have been detected and independently analysed in Section 3.1. Across the different K_a-ladder lines of HNCO, it is noted that some of them are more sensitive to the presence of the outflow. In order to illustrate that, and considering the case of HNCO lines affected by an outflow in the circumstellar envelope of the late star OH 231.8+4.2 (Velilla Prieto et al. 2015), we examine in detail two HNCO lines in G331.

We obtained Gaussian fit parameters for the identified HNCO lines. The results are presented in Table 1, where we list both the spectroscopic and fit parameters with their respective uncertainties. Concerning the HNCO line intensities and integrated areas, their values decrease inversely with the K_a ladder number, as it was also discussed in previous observational studies (Churchwell et al. 1986; Zinchenko et al. 2000; Velilla Prieto et al. 2015). While the HNCO $K_a = 0$ lines are strong enough to be detected, those with $K_a = 2$ require a more carefully analysis due to the weakness of the emission. We have performed the line identification adopting three standard criteria (e.g. Snyder et al. 2005), namely: (a) the agreement between the rest frequency of an assigned transition with the frequency at the local source rest velocity of the source, which for G331 is $V_{lsr} \simeq -90$ km s^{-1}; (b) lines with signal-to-noise ratio over the limit of detection (>3σ); (c) considering the relative intensities of predicted lines, e.g. under LTE conditions, and comparing with previous observational studies.

3.1 Qualitative analysis

3.1.1 *HNCO* $K_a = 0$

Nine lines of HNCO $K_a = 0$ have been detected and are exhibited in Fig. 1. They have been identified by selecting and superposing only HNCO $K_a = 0$ transitions over the spectral survey. The line intensities of those transitions are the highest in comparison to the $K_a = 1$, 2, and even 3 ladders. Examining the spectra, an antenna temperature value around 0.6 K could differentiate the HNCO K_a ladders, while $K_a = 1$, 2, and 3 exhibited $T_a \lesssim 0.6$ K. As a general perception in the observed K_a ladders, the intensities seem to be in reasonably agreement with the line strengths (i.e. Einstein coefficients) found in spectroscopic databases (Section 2), since they present a slight increment as a function of the frequency. That tendency can also be appreciated in Table 1, where we present the spectroscopic properties and estimated fluxes (i.e. integrated intensities) of the HNCO lines.

Among all the spectral lines, only two are likely affected by blended or contaminant emission.Those are the $11_{0,11}$–$10_{0,10}$, and $13_{0,13}$–$12_{0,12}$ transitions identified at 241 774.032 and 285 721.951 MHz, respectively (see Fig. 1). For the first one, two neighbour lines of CH_3OH, appearing at 241 767.247 MHz ($5_{-1,5}$ – $4_{-1,4}$ E) and 241 791.367 MHz ($5_{0,5} - 4_{0,4}$, A), are likely responsible for the blending. Those transitions were reported in previous works by Loren & Mundy (1984) in OMC-1. For the second one, it was found partially blended by a broad line likely associated to SO_2 v = 0 ($17_{3,15} - 17_{2,16}$) at the frequency ∼285 743 MHz.

Table 1 lists the spectroscopic properties of all the HNCO transitions. The first part of that table presents the HNCO $K_a = 0$ spectral characterization. The lowest and highest $K_a = 0$ transitions are HNCO $8_{0,8}$–$7_{0,7}$ and $16_{0,16}$–$15_{0,15}$ identified at the frequencies ∼ 175 843.695 and 351 633.257 MHz, respectively. Likewise, the upper energy levels (E_u) and Einstein coefficients (A_{ul}) that govern those transitions are in the ranges E_u ∼ 37.98–143.46 K and A_{ul} ∼ (7.43–61.3)× 10^{-5} s^{-1}, respectively. Gaussian functions are used to fit parameters as fluxes, full width at half-maximum (FWHM) and V_{lsr} values, all of them in units of K km s^{-1}, km s^{-1}, and km s^{-1}, respectively. As presented in Table 1, the rest frequencies of the lines are well identified at $V_{lsr} \approx -90$ km s^{-1} and the linewidths present a low dispersion of FWHM values, between ∼5.5 and 6.7 km s^{-1}. Fluxes are found to be in the range ∼ 3.63–8.02 K km s^{-1}, with the highest values for the lines at highest frequencies, according to APEX SHeFI 2. For the mentioned range, the lowest and highest flux values correspond to HNCO $9_{0,9}$–$8_{0,8}$ and $15_{0,15}$–$14_{0,14}$ at 197 821.461 and 329 664.367 MHz, respectively.

3.1.2 *HNCO* $K_a = 1$

17 lines of HNCO $K_a = 1$ have been observed as spectral pairs within the same rotational transitions. Their spectra are exhibited in Fig. 2. As we have already done for $K_a = 0$ ladder, $K_a = 1$ transitions have been chosen and superposed over the spectral survey. The intensities and fluxes of the $K_a = 1$ ladders are lower than those with $K_a = 0$. The $K_a = 1$ lines have been observed across a wide frequency interval, from ∼175 189.027 to 352 897.581 MHz, and they are stronger as the frequency increases. As we have highlighted for the $K_a = 0$ ladder, such tendency can be corroborated through the spectrum and

[3] http://www.apex-telescope.org/telescope/efficiency/
[4] https://www.iram.fr/IRAMFR/GILDAS/
[5] http://cassis.irap.omp.eu/
[6] http://physics.nist.gov/cgi-bin/micro/table5/start.pl
[7] https://www.astro.uni-koeln.de/cdms/catalog
[8] https://spec.jpl.nasa.gov/
[9] https://www.cv.nrao.edu/php/splat/

Downloaded from https://academic.oup.com/mnras/article/504/3/4428/6247604 by Universidad de Granada - Biblioteca user on 30 June 2021

Table 1. Lines of HNCO detected in G331. The transitions are presented following the order of the K_a-ladder numbers, $K_a = 0$, $K_a = 1$, and $K_a = 2$. The integrated flux (K km s^{-1}), line width (FWHM, km s^{-1}), and line position (V_{lsr}, km s^{-1}) are estimated from Gaussian fits.

Frequency (MHz)	Transition $(J_{k_a,k_c})_u - (J_{k_a,k_c})_l$	A_{ul} (10^{-5} s^{-1})	E_u (K)	Integrated flux (K km s^{-1})	FWHM (km s^{-1})	V_{lsr} (km s^{-1})	NIST reference
175 843.695	$8_{0,8} - 7_{0,7}$	7.43	37.98	3.71 ± 0.03	5.91 ± 0.05	− 90.23 ± 0.02	–
197 821.461	$9_{0,9} - 8_{0,8}$	10.70	47.47	3.63 ± 0.03	5.86 ± 0.07	− 90.36 ± 0.03	–
219 798.274	$10_{0,10} - 9_{0,9}$	14.70	58.02	4.53 ± 0.05	5.53 ± 0.07	− 90.50 ± 0.03	[1]
241 774.032	$11_{0,11} - 10_{0,10}$	19.60	69.62	5.35 ± 0.33	5.71 ± 0.44	− 90.47 ± 0.17	[3]
263 748.625	$12_{0,12} - 11_{0,11}$	25.60	82.28	4.86 ± 0.08	5.95 ± 0.12	− 90.66 ± 0.04	[1]
285 721.951	$13_{0,13} - 12_{0,12}$	32.60	95.99	7.90 ± 0.10	6.70 ± 0.10	− 90.76 ± 0.04	–
307 693.905	$14_{0,14} - 13_{0,13}$	40.90	110.76	7.24 ± 0.03	6.07 ± 0.03	− 90.56 ± 0.01	–
329 664.367	$15_{0,15} - 14_{0,14}$	50.40	126.58	8.02 ± 0.07	6.42 ± 0.08	− 90.64 ± 0.03	–
351 633.257	$16_{0,16} - 15_{0,15}$	61.30	143.46	6.79 ± 0.06	6.60 ± 0.08	− 90.51 ± 0.03	[7]
175 189.027	$8_{1,8} - 7_{1,7}$	7.16	81.11	1.01 ± 0.01	5.08 ± 0.07	− 90.93 ± 0.03	–
176 472.191	$8_{1,7} - 7_{1,6}$	7.31	81.39	0.76 ± 0.01	4.60 ± 0.10	− 90.97 ± 0.03	–
197 085.416	$9_{1,9} - 8_{1,8}$	10.30	90.57	0.68 ± 0.01	4.42 ± 0.08	− 90.99 ± 0.03	–
198 528.881	$9_{1,8} - 8_{1,7}$	10.50	90.92	1.01 ± 0.01	5.60 ± 0.10	− 90.85 ± 0.04	–
218 981.009	$10_{1,10} - 9_{1,9}$	14.20	101.08	1.75 ± 0.05	5.73 ± 0.21	− 90.67 ± 0.07	[1]
220 584.751	$10_{1,9} - 9_{1,8}$	14.50	101.50	1.73 ± 0.06	6.29 ± 0.31	− 90.79 ± 0.10	[2]
240 875.727	$11_{1,11} - 10_{1,10}$	19.00	112.64	1.56 ± 0.03	5.48 ± 0.12	− 90.91 ± 0.05	[3]
242 639.704	$11_{1,10} - 10_{1,9}$	19.50	113.15	1.74 ± 0.04	5.52 ± 0.13	− 90.67 ± 0.05	[3]
262 769.477	$12_{1,12} - 11_{1,11}$	24.80	125.25	1.80 ± 0.10	5.80 ± 0.50	− 90.80 ± 0.20	–
264 693.655	$12_{1,11} - 11_{1,10}$	25.40	125.85	1.59 ± 0.04	5.21 ± 0.19	− 90.85 ± 0.07	[4]
284 662.172	$13_{1,13} - 12_{1,12}$	31.70	138.91	2.13 ± 0.03	5.30 ± 0.10	− 90.86 ± 0.04	–
286 746.514	$13_{1,12} - 12_{1,11}$	32.40	139.61	2.53 ± 0.02	5.53 ± 0.06	− 90.91 ± 0.02	–
306 553.733	$14_{1,14} - 13_{1,13}$	39.70	153.62	2.13 ± 0.02	5.91 ± 0.07	− 90.86 ± 0.02	–
308 798.184	$14_{1,13} - 13_{1,12}$	40.60	154.43	2.74 ± 0.02	5.83 ± 0.07	− 90.86 ± 0.02	–
330 848.569	$15_{1,14} - 14_{1,13}$	50.10	170.31	4.64 ± 0.05	7.40 ± 0.10	− 90.56 ± 0.04	[5]
350 333.059	$16_{1,16} - 15_{1,15}$	59.70	186.20	3.24 ± 0.04	5.84 ± 0.09	− 90.81 ± 0.03	[6]
352 897.581	$16_{1,15} - 15_{1,14}$	61.00	187.25	2.55 ± 0.03	5.25 ± 0.08	− 90.81 ± 0.03	–
175 791.267	$8_{2,7} - 7_{2,6}$	6.65	208.25	0.37 ± 0.01	7.60 ± 0.30	− 92.20 ± 0.10	–
175 792.957	$8_{2,6} - 7_{2,5}$	6.65	208.25	0.41 ± 0.03	7.90 ± 0.60	− 89.40 ± 0.30	–
197762.939	$9_{2,8} - 8_{2,7}$	9.66	217.74	0.51 ± 0.02	9.10 ± 0.40	− 92.50 ± 0.20	–
197765.372	$9_{2,7} - 8_{2,6}$	9.66	217.74	0.52 ± 0.05	9.20 ± 0.40	− 88.8 ± 0.10	–
219733.850[†]	$10_{2,9} - 9_{2,8}$	13.50	228.29	–	–	–	[3]
219737.193[†]	$10_{2,8} - 9_{2,7}$	13.50	228.29	–	–	–	[3]
241703.852[a]	$11_{2,10} - 10_{2,9}$	18.10	239.89	–	–	–	–
241708.312	$11_{2,9} - 10_{2,8}$	18.10	239.89	0.67 ± 0.04	4.90 ± 0.40	− 91.20 ± 0.10	–
285640.923	$13_{2,12} - 12_{2,11}$	30.40	266.25	0.63 ± 0.05	6.40 ± 0.60	− 91.60 ± 0.20	–
285648.301	$13_{2,11} - 12_{2,10}$	30.40	266.25	0.53 ± 0.04	6.20 ± 0.60	− 91.30 ± 0.1	–
307607.799	$14_{2,13} - 13_{2,12}$	38.20	281.01	0.64 ± 0.02	7.70 ± 0.40	− 91.70 ± 0.1	–
307617.020	$14_{2,12} - 13_{2,11}$	38.20	281.01	0.47 ± 0.02	6.10 ± 0.30	− 90.70 ± 0.10	–
329573.452	$15_{2,14} - 14_{2,13}$	47.20	296.83	0.57 ± 0.05	5.50 ± 0.60	− 91.30 ± 0.20	–
329584.800	$15_{2,13} - 14_{2,12}$	47.20	296.83	0.64 ± 0.08	7.00 ± 1.00	− 90.8 ± 0.30	–
351537.795	$16_{2,15} - 15_{2,14}$	57.50	313.70	0.72 ± 0.07	5.80 ± 0.70	− 91.60 ± 0.20	–
351551.573	$16_{2,14} - 15_{2,13}$	57.50	313.70	0.46 ± 0.04	5.70 ± 0.70	− 90.80 ± 0.20	–

Notes and labels: Columns 5–7 list Gaussian fit parameters with their respective uncertainties.[†]Weak and unresolved lines. [a]Line likely affected by dominant emission of CH_3OH. NIST references, when available: [1] Armstrong & Loren (1984); [2] Loren & Mundy (1984); [3] Sutton et al. (1985); [4] Greaves & White (1991); [5] Sutton et al. (1991); [6] MacDonald et al. (1996); [7] Jewell et al. (1989).

the fitted parameters listed in the middle part of Table 1. Concerning to problems affecting the spectral emission, almost all the lines are clean or free of contamination.

Two aspects can be highlighted from the spectra exhibited in Fig. 2. On the one hand, the spectral profiles are not totally symmetrical, exhibiting a tail extended towards low-frequency values, in some cases. On the other hand, regarding contamination or problems in the spectra, the HNCO $10_{1,9}$–$9_{1,8}$ line at 220 584.751 MHz presents a neighbour unidentified emission that could be CH_3CN 12_6−11_6 at 220 594.431 MHz, which was previously reported in OMC-1 (Loren & Mundy 1984). Moreover, in the panel of the HNCO $12_{1,12}$−$11_{1,11}$ line at 262 769.477 MHz, a feature in absorption appears at ∼ 262 787 MHz affecting the whole spectrum. Such absorption is likely associated with water vapour as it has been discussed in studies about the atmospheric transparency at Chajnantor.[10]

Concerning the line profiles, the spectral tail mentioned above has also been evidenced in HNCO lines detected in OH 231.8+4.2, which is an oxygen-rich circumstellar envelope around an intermediate-mass evolved star also harbouring a bipolar molecular outflow (Velilla Prieto et al. 2015). So we speculate that such asymmetry in the lines could be due to outflow activity. In addition, it is also worth mentioning that such tail is more notorious in some transitions than others. It also seems to be better traced by the ladder $K_a = 1$

[10]https://almascience.eso.org/about-alma/atmosphere-model

Downloaded from https://academic.oup.com/mnras/article/504/3/4428/6247604 by Universidad de Granada - Biblioteca user on 30 June 2021

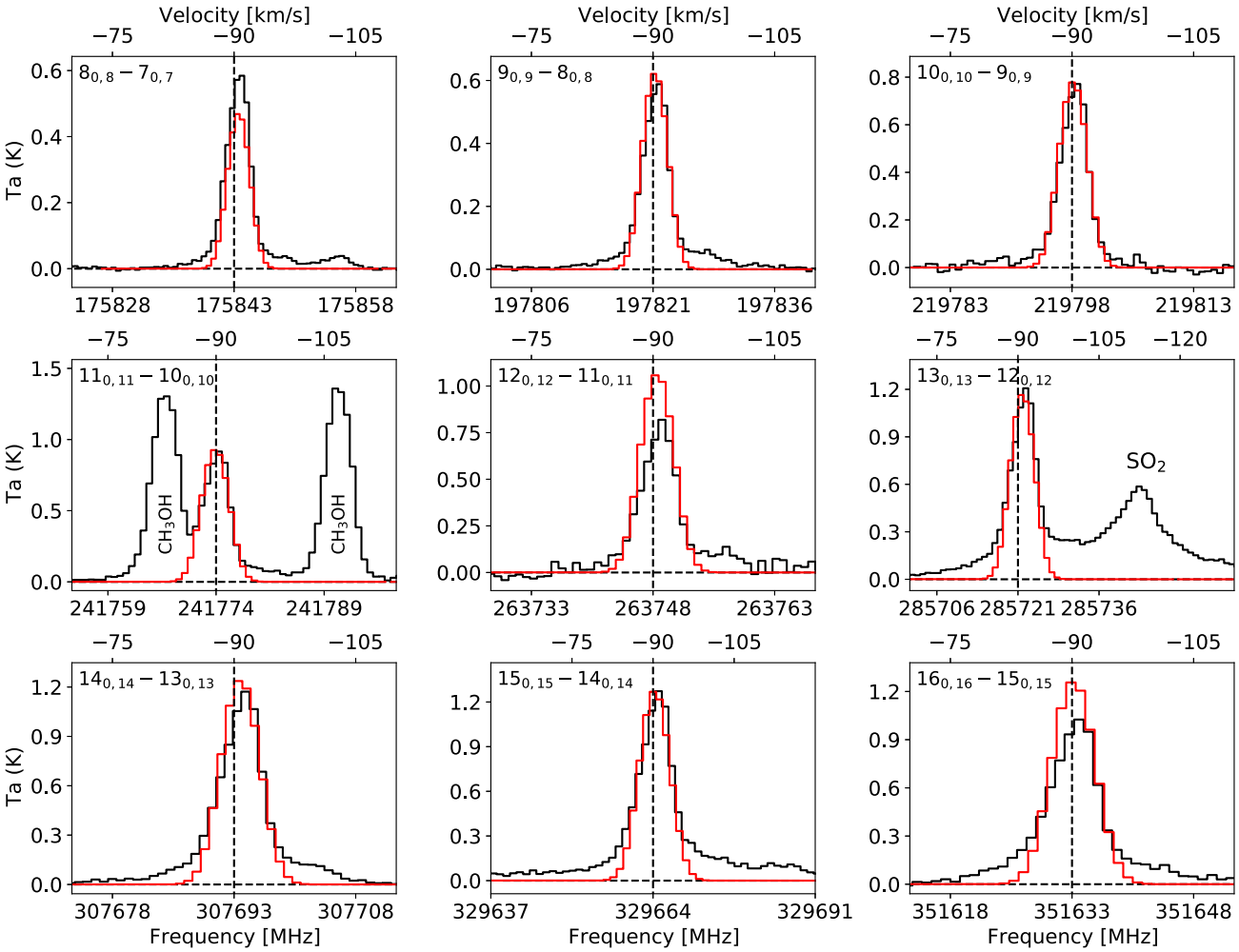

Figure 1. HNCO emission lines ($K_a = 0$) and their LTE models, exhibited as black and red histograms, respectively. The line intensities, *y*-axes, are given in units of antenna temperature, the *x*-axes represent the frequency (bottom) and velocity (top). The horizontal and vertical dashed lines represent the baseline and the rest velocity of G331, respectively. The transitions are indicated in the top left corner of each plot. The spectral resolution was smoothed to 1 km s^{-1}.

than $K_a = 0$. In Fig. 3, we emphasize the observed tails in the HNCO $8_{1,8}$–$7_{1,7}$ and $15_{1,14}$–$14_{1,13}$ lines, detected at 175 189.027 and 330 848.569 MHz, respectively, since both lines exhibit remarkably well the one-side tail extended up to −70 km s^{-1}. Comparing both lines, we note that the second one is more intense and stronger by a factor ∼5 if we take, for instance, the ratio from their fluxes. Although other studies found spectral profiles of HNCO (Velilla Prieto et al. 2015) similar to those observed here, we took into account a scenario of possible contamination affecting the HNCO emission (Fig. 3). However, such scenario is unlikely due to the rare species and/or transitions theoretically predicted. In the case of the HNCO $8_{1,8}$–$7_{1,7}$ line detected at 175 189.027 MHz, transitions of e.g. CH_2ND, C_2H_5OH, and i-C_3H_7CN are predicted at ∼175 185.19, 175 188.99, and 175 189.44 MHz. Regarding the HNCO $15_{1,14}$–$14_{1,13}$ line detected at 330 848.569 MHz, which was catalogued in Sgr B2(N) by Sutton et al. (1991), transitions of e.g. HCOCN and $^{15}NH_2HCO$ at ∼330 845.85 and 330 851.20 MHz, respectively, could be possible contaminants. Thus, the observed spectral profiles of HNCO seem to be much better explained by the outflow activity of G331.

In spite of the spectral asymmetries shown in Fig. 3, a relative percentage was estimated by considering the area under the Gaussian fits with respect to the whole area integrated within $-70 \leq V_{lsr}$(km s^{-1}) ≤ -110. Thus, the areas under the Gaussian fits represent up to ≈80 per cent of the total area under the spectra. Although these lines have different intensities and fluxes (Fig. 3b), the percentages are similar as both lines have similar spectral tails. Velilla Prieto et al. (2015) also observed this wing, through spectral lines of HNCO, but in outflows of AGB stars.

3.1.3 *HNCO* $K_a = 2$

16 transitions of HNCO $K_a = 2$ have been identified across the survey, they appear as spectral pairs partially resolved. The spectral lines are exhibited in Fig. 4, where it can be noted that their emission are noisier and weaker than the previously analysed K_a ladders; those were aspects that put constraints on the line identification of the HNCO $K_a = 2$ transitions. Likewise, it can be observed that the intensity of the lines increases with the frequency. In addition, the spectral pairs are more spaced as the frequency increases. For instance, by comparing the two panels centred at 175 792 and 329 579 MHz of Fig. 4, it can be noted that the spectral pair of the second one, $15_{2,14}$–$14_{2,13}$ and $15_{2,13}$–$14_{2,12}$, is better resolved than the first one, $8_{2,7}$–$7_{2,6}$ and $8_{2,6}$–$7_{2,5}$. Apart from the HNCO blending mentioned above, only the $K_a = 2$ transitions at ∼241 706 MHz are

Downloaded from https://academic.oup.com/mnras/article/504/3/4428/6247604 by Universidad de Granada - Biblioteca user on 30 June 2021

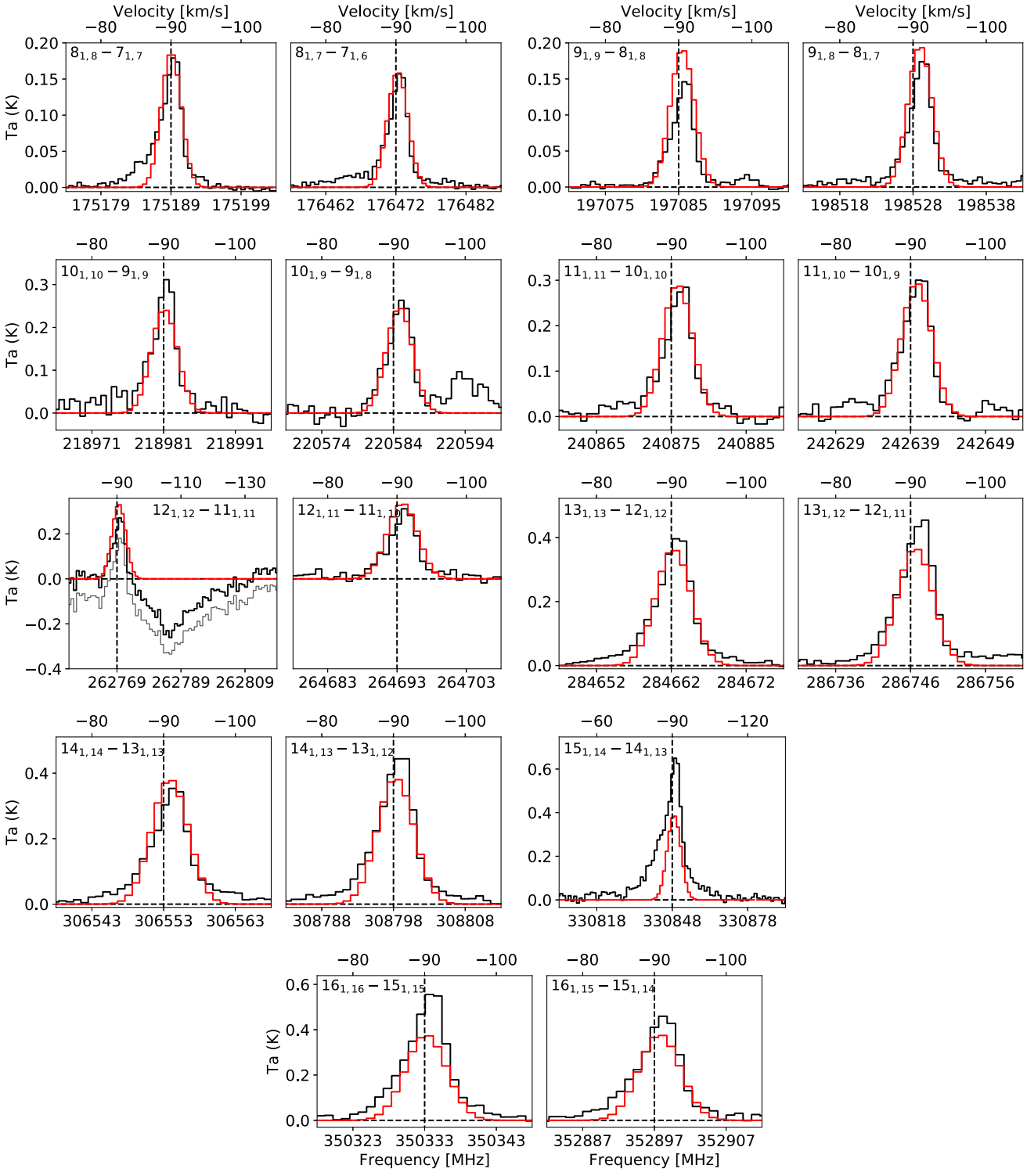

Figure 2. As in the caption of Fig. 1. HNCO emission lines ($K_a = 1$) and their LTE models. The transitions are indicated in the top left corner of each plot. In the panel of the $12_{1,12} - 11_{1,11}$ line at ∼262 769 MHz, the black spectrum was adjusted from the grey one which is likely compromised by an atmospheric issue at ∼262 785 MHz (see the text).

affected by a neighbour and intense line of CH_3OH ($5_{0,5}$–$4_{0,4}$, E) identified at ∼ 241 700 MHz (see Fig. 4). Concerning the line profiles, the lines do not exhibit the spectral tails like those highly evidenced in the HNCO $K_a = 1$ ladder.

In the lowest part of Table 1, we present the parameters of the observed HNCO $K_a = 2$ transitions. Summarizing, the lowest and highest transitions are identified at the rest frequencies 1757 91.267 and 351 551.573 MHz, respectively. Their upper energy levels, which are in the range E_u ∼ 208.25–313.70 K, are the highest in comparison with the other K_a ladders. Concerning the Einstein coefficients, they are in the range A_{ul} ∼ (6.65–57.5)× 10^{-5} s^{-1}, similar to those of the other K_a ladders. In order to quantify the spectral emission, Gaussian

Downloaded from https://academic.oup.com/mnras/article/504/3/4428/6247604 by Universidad de Granada - Biblioteca user on 30 June 2021

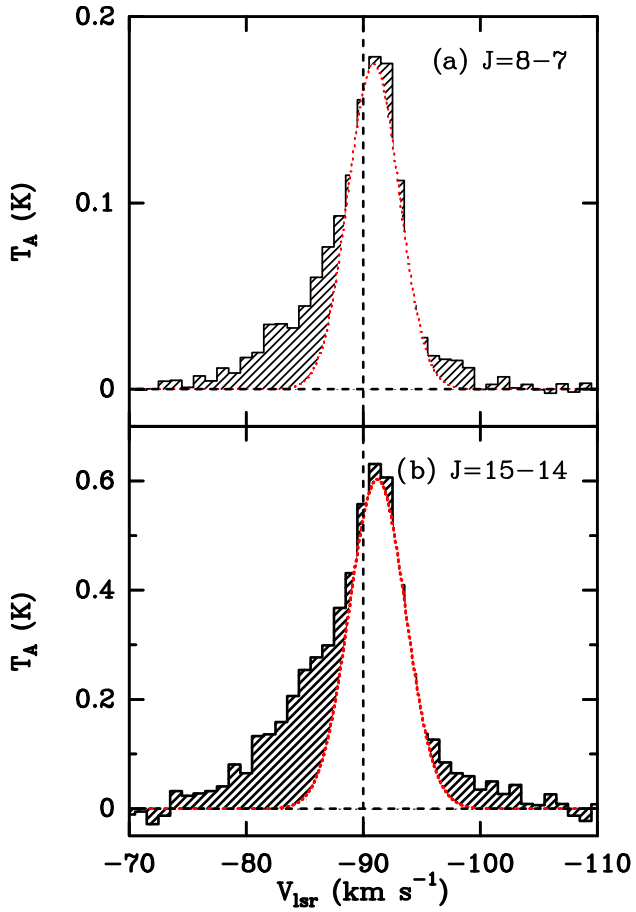

Figure 3. Spectral wings observed in the (a) HNCO $8_{1,8}$–$7_{1,7}$ and (b) $15_{1,14}$–$14_{1,13}$ transitions identified at the rest frequencies ∼175 189.027 and 330 848.569 MHz, respectively. The diagonal patterns depict the area under the spectra from −70 to −110 km s^{-1}. The red dotted lines depict the areas under the Gaussian fits.

functions have been adjusted to estimate the line parameters, whose results are presented in Table 1. Since the lines are partially blended, the estimation of the Gaussian fits has been difficult, mainly for the lowest frequency transition pairs observed at ∼ 175 792, 197 764, 219 735, and 241 706 MHz. In addition to that problem, and due to the weakness of the emission, the resultant Gaussian fits are not as good as those for the previously analysed K_a ladders; as a consequence, the LTE analysis of the HNCO $K_a = 2$ lines, e.g. the match between models and observations (Fig. 4), might not be as reliable as those obtained from the strongest K ladders observed in this work (Figs 1 and 2). Regarding the rest frequencies, they were found more dispersed with respect to the systemic velocity, approximately between −88 and −92 km s^{-1}. Intensities and fluxes were found to be as the weakest among all the K_a ladders, see Table 1. The transitions $10_{2,9}$–$9_{2,8}$, $10_{2,8}$–$9_{2,7}$, and $11_{2,10}$–$10_{2,9}$ were unable to obtain reliable Gaussian fits.

3.1.4 *HNCO* $K_a = 3$

A subtle evidence for a HNCO $K_a = 3$ line has been found. The HNCO $13_{3,10}$–$12_{3,9}$ transition is identified at the rest frequency 285 541.575 MHz, and is exhibited in Fig. 5. As expected, the spectral line is weak and has the highest upper energy level identified in this work, $E_u = 470.91$ K, with $A_{ul} = 2.78 \times 10^{-4}$ s^{-1}. As a consequence, such emission would suggest a higher excitation condition than that found from the other HNCO $K_a = 0$, 1, and 2 ladders. As can be noted by the models at two different excitation temperatures displayed in Fig. 5, the highest temperature does reproduce better the line profile. Analysing other species for the peak, CH_3OCN at 285 539.098 MHz, DNCO at 285 539.531 MHz, or acetone $(CH_3)_2CO$ at 285 542.349 MHz could be candidate transitions. The predicted position in the spectrum for those species are also indicated in Fig. 5.

3.2 LTE analysis

In order to estimate the physical conditions traced by HNCO in G331, we constructed rotational diagrams. They are an important method to infer source properties from molecular line emissions (see Goldsmith & Langer 1999, for a complete description and discussion). They basically consist of a plot of the column density per statistical weight, for a given number of molecular rotational energy levels, as a function of their energies above the ground state. More specifically, if LTE is assumed for the source, the level populations can be represented by the Boltzmann distribution and the rotational diagram is described by equation (1). Moreover, if the emission lines can also be considered as optically thin, the plotted function is a straight line with a slope defined by $1/T_{ex}$ from which is possible to derive the excitation temperature of the source where it is the molecule, which should be equal to the kinetic temperature of the gas in LTE conditions. Thus,

$$\ln\left(\frac{N_u}{g_u}\right) = \ln\left(\frac{3kW}{8\pi^3 \nu S_{ul} \mu^2 g_u}\right) = \ln\left(\frac{N}{Q}\right) - \frac{E_u}{k\,T_{ex}} \quad (1)$$

where N_u is the column density of the upper level, g_u the degeneracy of the upper level, k is the Boltzmann constant, W the integrated intensity of the transition, ν the rest frequency of the line, S_{ul} is the line strength of the transition, μ is the dipolar moment, N is the total column density, Q is the internal partition function of the molecule, and E_u the upper level energy of the transition.

For the construction of the rotational diagram, it is also considered a beam dilution factor associated with a point-like emitter region. The correction can be performed by the addition of the term $\ln(\Delta\Omega_a/\Delta\Omega_s)$ on the right-hand side of equation (1; Goldsmith & Langer 1999), where $\Delta\Omega_a$ is the antenna solid angle and $\Delta\Omega_s$ is the source solid angle. This ratio correlates the subtended angle of the source with the solid angle of the antenna beam. For the HNCO emission, observed through several spectral lines, we adopt a hypothetical source size of 5 arcsec to evaluate the beam dilution effects, although, under the hypothesis that the emission fills the antenna beam, a rotational diagram solution was also constructed considering 30 arcsec. The LTE treatment of HNCO was motivated by radiative analyses of HC_3N in G331, although the physico-chemical origin of both molecules is different. For instance, in previous works, various lines of HC_3N, including its ^{13}C isotopologues, were analysed with *APEX* (Duronea et al. 2019), as well as mapped with *ALMA* via the HC_3N $J = 38$–37 transition (Hervías-Caimapo et al. 2019). Furthermore, in the case of optically thick transitions, the optical depth correction can be performed by the correction factor C_τ (equation 3) as shown in equation (2; as derived in Goldsmith & Langer 1999):

$$N_{u,thick} = N_{u,thin} \times C_\tau \quad (2)$$

$$C_\tau = \frac{\tau}{1 - e^{-\tau}}, \quad (3)$$

where τ is the optical depth.

The rotational diagrams with and without opacity correction (2) are presented in Fig. 6. Regarding the rotational diagram corrected

Downloaded from https://academic.oup.com/mnras/article/504/3/4428/6247604 by Universidad de Granada - Biblioteca user on 30 June 2021

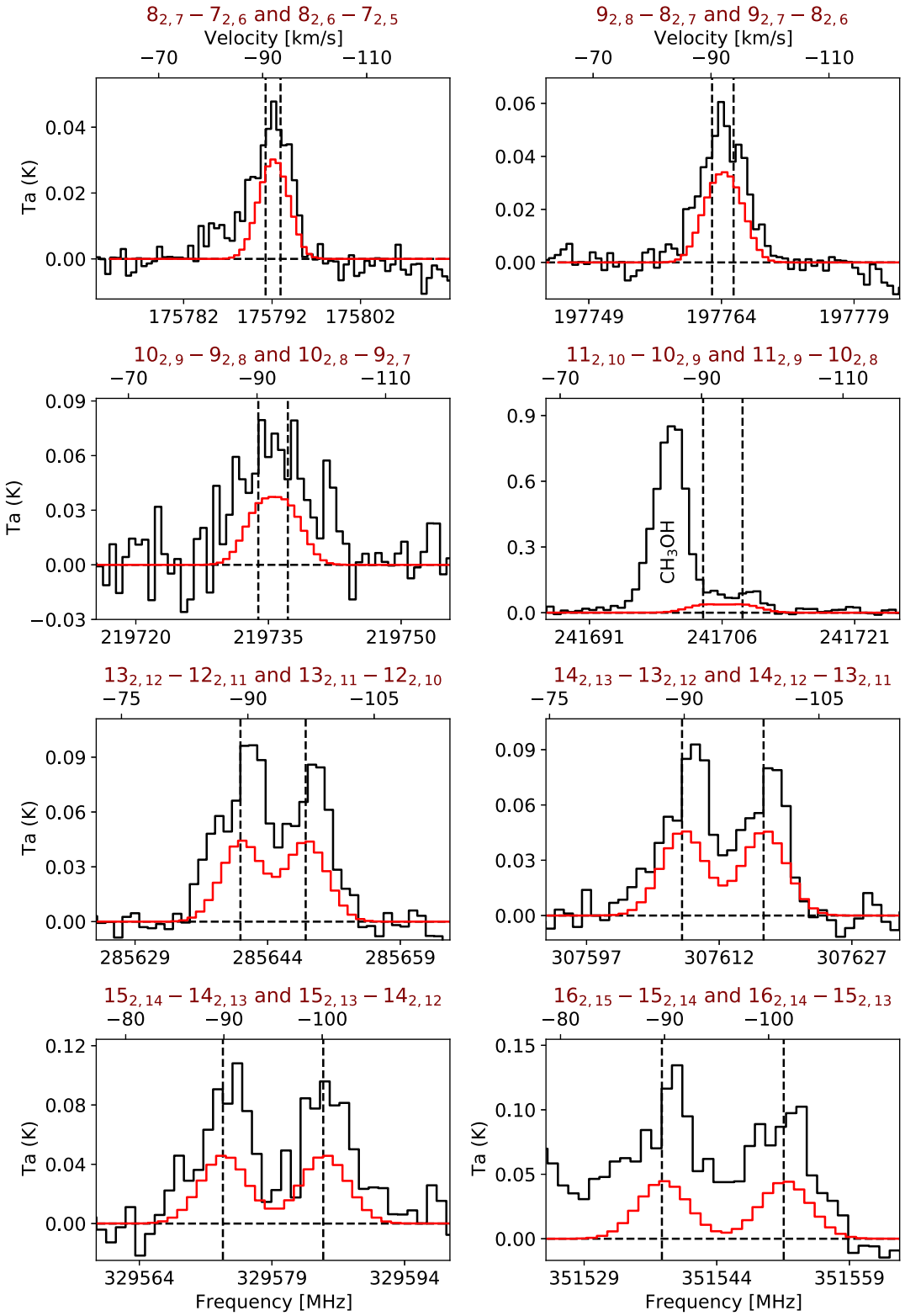

Figure 4. As in the caption of Fig. 1. HNCO emission lines ($K_a = 2$) and their LTE models. The transitions are indicated in the top left corner of each plot.

by the opacity, it considers only the non-blended transitions of HNCO because the opacity correction does not converge on blended transitions, like various of those belonging to the $K_a = 2$ ladder and identified at lowest frequency values (e.g. the first panels of Fig. 4). The best linear fit for the diagrams gave $N(\mathrm{HNCO}) = (3.1 \pm 0.4) \times 10^{15}$ cm^{-2} and $T_{ex} = 59.4 \pm 2.3$ K, without the opacity correction; and $N(\mathrm{HNCO}) = (3.7 \pm 0.5) \times 10^{15}$ cm^{-2} and $T_{ex} = 58.8 \pm 2.7$ K, by applying the opacity correction. The reduced χ^2 values for each fit are 1.12 and 1.21, respectively. Assuming that the HNCO emission is extended, optically thin, and that fills approximately the antenna

Downloaded from https://academic.oup.com/mnras/article/504/3/4428/6247604 by Universidad de Granada - Biblioteca user on 30 June 2021

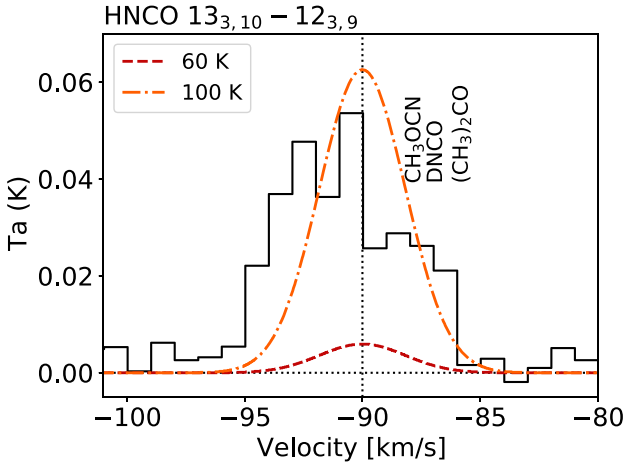

Figure 5. Tentative detection of the HNCO line ($13_{3,10} - 12_{3,9}$) at the rest frequency 285 541.575 MHz. The baseline and the source's velocity are represented by the dotted horizontal and vertical lines, respectively. The LTE models at 60 and 100 K, displayed as red dashed and orange dot–dashed lines, respectively, are to illustrate the rotational diagram result and a hypothetical higher excitation condition, respectively. There is a fainter emission next to the HNCO line where we indicated other candidate molecules.

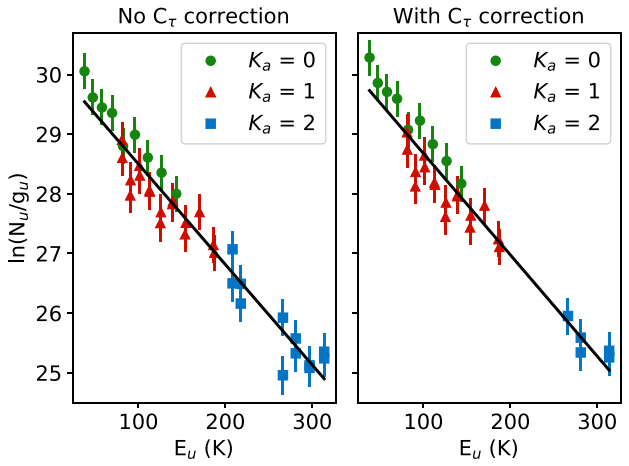

Figure 6. Rotational diagrams of HNCO constructed applying opacity correction (right-hand panel) and without opacity correction (left-hand panel). In both cases, a source size of 5 arcsec was adopted. In second plot, only the lines with no blended/contaminant emission are considered. The best linear fit for each display yields, respectively, $T_{ex} = 59.4 \pm 2.3$ K and $N = (3.1 \pm 0.4) \times 10^{15}$ cm^{-2} (χ^2_{red}=1.12); and T_{ex}= 58.8 ± 2.7 K and $N = (3.7 \pm 0.5) \times 10^{15}$ cm^{-2} (χ^2_{red}=1.21). The set of data with different K_a values are also represented in the plots.

beam, we evaluated a rotational diagram adopting 30 arcsec, the best linear fit (χ^2_{red}=1.98) gave N(HNCO) = (1.4 ± 0.2) × 10^{14} cm^{-2} and T_{ex}= 65.5 ± 3.7 K. With similar results, such temperatures around 60 K might indicate that HNCO molecules are concentrated in external and colder regions of the core, according to the proposed shell-like structure of G331 (Merello et al. 2013b; Duronea et al. 2019; Hervías-Caimapo et al. 2019).

Moreover, Churchwell et al. (1986) indicated that HNCO transitions with $E_u > 40$ K require an excitation temperature of ∼70 K and also that radiative processes are responsible for the excitation of HNCO in Sgr B2, as already mentioned. This suggests that HNCO can be considered as a good probe of the far-infrared radiation field but not of gas properties such as density and kinetic temperature. The only common transition with our work is $10_{0,10}$–$9_{0,9}$, the others are at lower frequencies (Churchwell et al. 1986). In this sense, according to the similar excitation temperature of ∼60 K obtained with the rotational diagrams, the same trend appears to be maintained at higher HNCO transition levels. This may imply that radiative processes, rather than collisional mechanisms, could also dominate the excitation of HNCO molecules in G331. In this article, it is reported for first time a multiline analysis of HNCO, covering transitions within the energy interval $E_u \approx$ 37–314 K, towards a massive hot molecular core/outflow like G331. Recently, He et al. (2021) studied the spatial distribution of HNCO $4_{0,4}$–$4_{0,3}$, SiO 2–1, and HC_3N 10–9 in a sample of southern massive star-forming regions, discussing correlations between the morphology of the gas and dust emission. In an earlier work, Martín et al. (2008) proposed how HNCO and CS could be useful molecules to study the influence of shocks and/or the radiation field in nuclear regions of galaxies. Thus, there are follow-up questions that warrant further studies to have a deeper understanding on the role that the outflow activity, the physical conditions of the dust, and collisional mechanisms can play into the formation, distribution, and excitation of HNCO gas in massive protostellar objects like G331.

4 DISCUSSION

4.1 Abundances: comparison with other sources

From the column densities obtained with the rotational diagram, assuming a source size of 5 arcsec, it is possible to estimate the abundance of HNCO if the column density of H_2 is also known. The most recent values of $N(H_2)$ derived for G331 are 9.7 × 10^{23} cm^{-2}, obtained from the $H^{13}CO^+/H_2$ ratio of Orion KL, and 2.7 × 10^{23} cm^{-2}, estimated by the superficial density from the continuum emission at 1.2 mm in G331 (Duronea et al. 2019, and references therein). Therefore, by taking the column density of HNCO corrected by the optical depth, N(HNCO)=(3.7 ± 0.5) × 10^{15} cm^{-2}, and adopting H_2 column densities values of 2.7 × 10^{23} and 9.7 × 10^{23} cm^{-2}, the relative abundances of HNCO are estimated to range from (3.8 ± 0.5) × 10^{-9} to (1.4 ± 0.2) × 10^{-8}.

In Fig. 7, the histograms of the column densities and HNCO abundances for several sources are displayed in order to compare with those derived for G331. The objects shown are high-mass young stellar objects (YSOs) in hot core stages (AFGL 2591, G24.78, G75.78, NGC 6334 IRS1, NGC 7538 IRS1, W3(H2O), and W 33A; Bisschop et al. 2007); low-mass protostar IRAS 16293–2422, in the compact source B (Martín-Doménech et al. 2017) and in the hot corino region (Hernández-Gómez et al. 2019); oxygen-rich circumstellar envelope around an intermediate-mass evolved star (OH231.8+4.2; Velilla Prieto et al. 2015); and hot molecular core (G10.47+0.03; Gorai et al. 2020).

Concerning the HNCO column densities, G331 and most of the YSOs of Bisschop et al. (2007) present similar values. This might be due to similar evolutionary stage of these objects, with protostars embedded in hot molecular cores. The two sources of IRAS 16293–2422 have higher column densities, which could be connected to the innermost and densest regions of this object (e.g. hot corino). In colder envelopes, the HNCO column densities could be up to four orders of magnitude lower (Hernández-Gómez et al. 2019). The histogram of the abundances, on the other hand, reveals a greater variation among the objects. The HNCO abundances of G75.78 and $G331_{MIN}$ are very similar, while $G331_{MAX}$ is in better agreement with the other YSOs.

Downloaded from https://academic.oup.com/mnras/article/504/3/4428/6247604 by Universidad de Granada - Biblioteca user on 30 June 2021

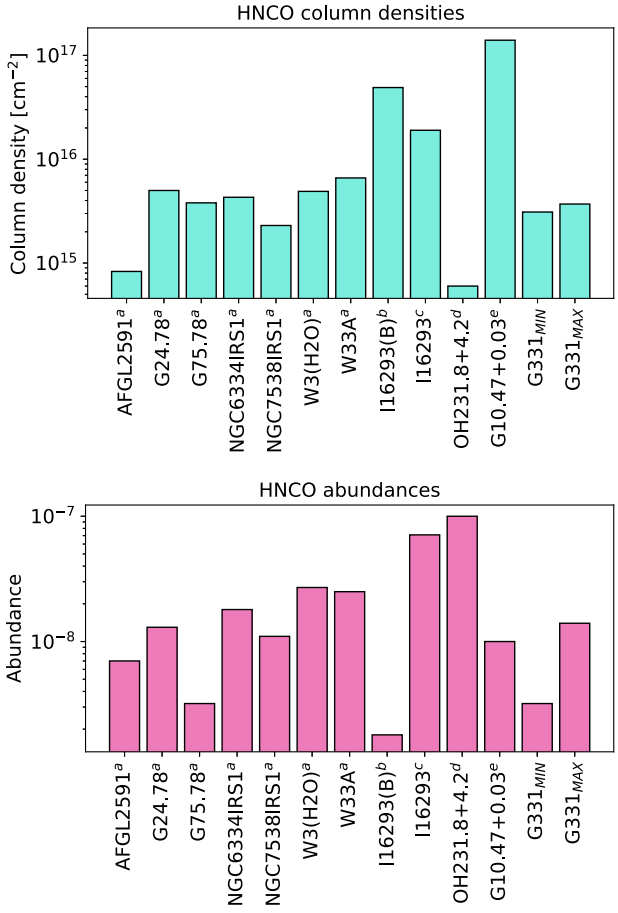

Figure 7. Histograms of the column densities of HNCO (top) and their relative abundances to H_2 (bottom) in several sources: [a]Bisschop et al. (2007), [b]IRAS 16293–2422 (B, Martín-Doménech et al. 2017), [c]IRAS 16293–2422 (*hot corino*, Hernández-Gómez et al. 2019), [d]Velilla Prieto et al. (2015), [e]Gorai et al. (2020). The minimum and maximum values (G331$_{MIN}$ and G331$_{MAX}$) obtained for G331 are also shown.

It is worth noting that the column density reported for G10.47+0.03 is much higher than G331, however the abundance of HNCO in this source is in the range calculated for G331. The most evolved object in this sample, OH231.8+4.2, shows the lowest column density and the highest abundance of HNCO. Despite these peculiar cases, the values of HNCO column density and abundance in G331 are in agreement with those obtained in most of the hot molecular cores in the histograms.

4.2 The CHNO isomers: HNCO, HOCN, HCNO, and HONC

HNCO has three meta-stable isomers of which HCNO (fulminic acid) and HOCN (cyanic acid) as well as HNCO have been observed in the ISM. Isofulminic acid (HONC) is the only meta-stable isomer that has not been detected in the ISM yet. All these isomers are quasi-linear molecules except isofulminic acid, which has a bent structure (Mladenovic & Lewerenz 2008; Mladenovic et al. 2009). HCNO and HOCN are much less abundant than HNCO and their occurrence in space has been restricted to a few sources. On the one hand, HCNO was discovered in dark clouds by Marcelino et al. (2009); using observations at the 3 mm band of the *IRAM*-30 m telescope, they detected HCNO in the starless cores B1, L1544, L183 as well as in the low-mass star-forming region L1527. On the other hand, HOCN was observed towards the Galactic centre by Brünken et al. (2010); similarly, using observations at the 3 mm band of *IRAM*-30 m, they detected transitions of HOCN in a quiescent molecular cloud and in several positions of the Sgr B2 complex.

The dipole moments of the four isomers have been reported and discussed in the literature. The values for HNCO, HCNO, HOCN, and HONC have been estimated to be ∼2.08, 3.1, 3.7, and 3.13 D, respectively (e.g. Hocking et al. 1974; Hocking et al. 1975; Takashi, Tanaka & Tanaka 1989; Mladenovic & Lewerenz 2008; Mladenovic et al. 2009). Among the four species, HNCO is the most stable one (by 1.1 eV), this has been demonstrated through studies about the equilibrium structure and energetic of the CHNO isomers (e.g. Mladenovic & Lewerenz 2008; Mladenovic et al. 2009). Regarding the abundance ratios between the isomers, Marcelino et al. (2009) determined HNCO/HCNO between 40 and 70 in dark clouds and starless cores; Brünken et al. (2010) determined values of ∼ 0.3–0.8 per cent for HOCN relative to HNCO towards the Galactic centre.

In this work, HNCO was clearly detected through several spectral lines, as presented in Table 1. The search for HCNO and HOCN, on the other hand, did not yield conclusive results to confirm their presence in G331. About HOCN, the number of predicted transitions with $E_u < 450$ K is about 60; however, only spectral noise has been observed where most of the lines should appear. Two transitions might be speculatively inspected since they are dominated by spectral emission relatively well known in the literature. That is the case of the transition HOCN $9_{3,6}$–$8_{3,5}$ at the rest frequency 188 655.358 MHz, which is likely affected by SO_2 $9_{2,8}$–$9_{1,9}$ at 188 654.973 MHz; and HOCN $12_{3,10}$–$11_{3,9}$ at the rest frequency 251 528.269 MHz, which is likely affected by c-C_3H_2 $6_{2,5}$–$5_{1,4}$ at 251 527.311 MHz (Nummelin et al. 1998). Regarding HCNO, the number of predicted transitions is considerably minor in comparison to HOCN, about 10 for the same interval of E_u. Similarly, the transition HCNO 12–11 is identified at the rest frequency 275 227.774 MHz, however it is likely affected by SO_2 $15_{3,13}$–$15_{2,14}$ at 275 240.184 MHz (Loren & Mundy 1984). Additionally, in the SO_2 case, a factor that also makes difficult a positive identification is that the lines exhibit Lorentzian profiles, so that such emission could be more related to the outflow. In the c-C_3H_2 case, the line exhibit a Gaussian profile as the HNCO lines, which could be more in agreement with the physical origin of the HNCO emission. In perspective, the 'puzzle' of the CHNO isomers in hot molecular cores is compelling, but theoretical and/or experimental approaches might be required for a better comprehension of such a chemical puzzle.

4.3 Internal partition function of CHNO isomers

The rotational-vibrational partition function of the isomers of CHNO (Section 4.2; McLean, Loew & Berkowitz 1977) have been updated in this work according to Carvajal et al. (2019) and presented here altogether for their comparison.

Usually, the internal partition function is computed as a direct sum of a considerable number of rovibrational energies in order to reach a convergence at any temperature. Unfortunately, the spectroscopic data for the isomers of CHNO is still insufficient. Then, we have to compute the partition function adopting some suitable approximations that were already validated (see e.g. Carvajal et al. 2019, and references therein). Thus, the molecular partition functions for CHNO isomers are computed as a product of the rotational partition function $Q_{\rm rot}(T)$ and of the vibrational contribution $Q_{\rm vib}(T)$:

$$Q_{\rm rv}(T) \approx Q_{\rm rot}(T)\, Q_{\rm vib}(T), \quad (4)$$

Downloaded from https://academic.oup.com/mnras/article/504/3/4428/6247604 by Universidad de Granada - Biblioteca user on 30 June 2021

where the rotational contribution is computed as a direct sum whether the convergence is reached with the available spectroscopic data. In the particular cases of the CHNO isomers, the rotational spectroscopic information is available in the CDMS catalogue and the predicted rotational energies in the vibrational ground state can be computed with Pickett's code (Pickett 1991). Otherwise, the approximation of the classical partition function can be a suitable alternative to provide the rotational partition function for sources at not very low temperatures (Herzberg 1991) besides being a useful tool to test the convergence of the direct sum at higher temperatures (Carvajal et al. 2019). In the particular cases of CHNO isomers, the classical partition function values turn out to be adequate at temperatures higher than 20 K. However, the addition of some simple correction terms to the classical partition function can improve this approximation considerably (Wells & Raston 2020). For all the CHNO isomers, the nuclear spin statistical weights are the same and, in this work, they are considered as 1.

Concerning the vibrational partition functions for the CHNO isomers, these cannot be obtained as a direct sum because there are not enough experimental or calculated vibrational energies at disposal. Therefore, the harmonic approximation (Herzberg 1991) has been used to estimate the vibrational contribution of the partition function and therefore it is enough to know the vibrational fundamental frequencies. If any bending degree of freedom for these four isomers was susceptible to undergo a strong anharmonicity caused, e.g. by a large amplitude motion, the vibrational partition function could be split into two contributions (see e.g. Carvajal et al. 2019, and references therein): the one derived from small amplitude vibrations and another coming from the large amplitude vibrational modes. The vibrational partition function from the small amplitude vibrations can be computed with the harmonic approximation whereas the large amplitude contribution should be calculated as a direct sum using the predicted energies of the large amplitude bending states (Favre et al. 2014), which could be calculated with any approach conceived for the analysis of nonrigid molecules (see e.g. Jensen 1983; Khalouf-Rivera, Pérez-Bernal & Carvajal 2020).

Table 2 provides, for the four CHNO isomers, the results of the vibrational contribution in the harmonic approximation ($Q_{\rm vib}^{\rm harm}$) of the internal partition function ($Q_{\rm rv}$), the internal partition function computed in the present work by means of equation (4), the rotational partition function in the CDMS catalogue computed as a direct sum (Endres et al. 2016), and the relative differences between the values reported in the present work and in the CDMS for the temperature range from 2.725 to 500 K. In addition, the uncertainties of the internal partition functions have been included for the four CHNO isomers. These have been estimated upwardly considering large uncertainties for the rotational and vibrational fundamental energies at 100 MHz and 1 $\rm cm^{-1}$, respectively. In general, at temperatures above 20 K, the relative difference between the partition function values obtained in the present work and those in CDMS catalogue are substantially larger than the upward estimate of the uncertainty of the internal partition function.

From Table 2, it can be observed that the rotational contributions to the internal partition functions of the four isomers have similar values at the lowest temperatures, e.g. down to $T = 10$ K. For higher temperatures, above $T = 225$ K, the difference between the rotational partition function of fulminic acid and the values of the other three isomers (isocyanic acid, cyanic acid, and isofulminic acid), with more similar values, becomes larger. This could be explained because of the structure of fulminic acid is linear and of the other have a near-prolate asymmetric top structure. Nevertheless, the internal partition functions of isocyanic acid, cyanic acid, and isofulminic acid become completely different at higher temperatures despite the fact that these three isomers have a bent structure. This stems from the differences among the vibrational partition functions of the bent isomers.

In Table 2, the weight of the vibrational contribution to the internal partition function can also be assessed for the set of the four CHNO isomers at different temperatures. The differences between the internal partition function and the rotational partition function become noteworthy (more than 1 per cent) at temperatures higher than 225 K for HNCO, 150 K for HOCN, and $T = 75$ K for HCNO and HONC. Even when the vibrational partition function has been calculated with the harmonic approximation and, in some cases, using fundamentals, the values of this approximation, although underestimated, are in good agreement with the direct sum values (Carvajal et al. 2019).

As supplementary material, the rotational, vibrational, and rovibrational partition function calculated in the present work from 1 to 500 K (in intervals of 1 K) is also provided for the following isomers: cyanic acid (HOCN); fulminic acid (HCNO); and isofulminic acid (HONC). For isocyanic acid (HNCO), same material can be found elsewhere (Carvajal et al. 2019).

In Appendix A, we will give some details about the calculation of the partition function for the four CHNO isomers.

4.4 Chemical modelling with NAUTILUS

In order to better understand the chemical pathways involved in the production and destruction of HNCO, we used the NAUTILUS code (Ruaud et al. 2016) to carry out a time-dependent chemical model. NAUTILUS allows to simulate and study grain- and gas-phase chemical processes for instance in hot and cold cores (Semenov et al. 2010; Reboussin et al. 2014; Ruaud et al. 2015, 2016). The predictions of the model include the time evolution of the chemical abundances for a given set of physical and chemical parameters. For the solid-state chemistry, it considers mantle and surface as chemically active, following the formalism of Hasegawa & Herbst (1993) and the experimental results of Ghesquière et al. (2015). In this sense, the code can perform a three-phase (gas plus grain mantle and surface) time-dependant simulation of the chemistry in hot cores, including chemical reactions in both gas and solid phases (Ruaud et al. 2015).

This approach is interesting for our work since most of HNCO may be trapped in icy grains, as suggested by Altwegg et al. (2020). The grain chemistry of the code considers the standard direct photodissociation by photons along with the photodissociation induced by secondary UV photons, as described by Prasad & Tarafdar (1983), which are effective processes on the surface and mantle of the grains. The network of chemical reactions used by the code is presented on the KInetic Database for Astrochemistry[11] catalogue (Wakelam et al. 2015).

The first and simplest simulation to perform is a zero-dimensional, i.e. total density, gas temperature, and other physical condition are uniform within the considered core and throughout the simulation time. There is no structure evolution in this case. Once our source present a shell-like structure, a more elaborated structure model is necessary to be simulated together with NAUTILUS in order to

[11] http://kida.obs.u-bordeaux1.fr/

Downloaded from https://academic.oup.com/mnras/article/504/3/4428/6247604 by Universidad de Granada - Biblioteca user on 30 June 2021

Table 2. Vibrational and rotational-vibrational partition function for CHNO isomers: isocyanic acid (HNCO); cyanic acid (HOCN); fulminic acid (HCNO); and isofulminic acid (HONC). Comparison between the values obtained in the present study and those published in CDMS catalogue[a].

	HNCO[b]				HOCN			
T(K)	Q_{vib}^{harm} [c]	Q_{rv}(Carvajal et al. 2019)[d]	Q(CDMS)[e]	Rel. diff.(%)[f]	Q_{vib}^{harm} [c]	Q_{rv}(Present work)[d, g]	Q(CDMS)[e]	Rel. diff.(%)[f]
2.725	1.000 000	5.5129(50)	5.51	0.00	1.000 000	5.7601(52)	5.7601	0.00
5.000	1.000 000	9.8228(42)	9.82	0.00	1.000 000	10.3038(44)	10.3038	0.00
9.375	1.000 000	18.4493(36)	18.45	0.00	1.000 000	20.1244(37)	20.1244	0.00
18.750	1.000 000	42.8295(30)	42.83	0.00	1.000 000	50.8161(32)	50.8159	0.00
37.500	1.000 000	117.3053(27)	117.30	0.01	1.000 000	142.1565(12)	142.1413	0.01
75.000	1.000 019	332.0002(27)	331.99	0.00	1.000 314	402.21(33)	401.3740	0.21
150.000	1.006 395	949.759(40)	943.71	0.64	1.024 660	1165.30(98)	1135.3539	2.57
225.000	1.048 753	1827.01(36)	1742.43	4.63	1.114 711	2328.9(22)	2087.4819	10.37
300.000	1.144 368	3080.9(12)	2695.34	12.51	1.269 376	4083.1(48)	3217.0765	21.21
500.000	1.667 813	9690.5(89)	5866.52	39.46	1.984 226	13733.(23)	–	–
	HCNO				HONC			
T(K)	Q_{vib}^{harm} [c]	Q_{rv}(Present work)[d]	Q(CDMS)[e]	Rel. diff. (%)[f]	Q_{vib}^{harm} [c]	Q_{rv}(Present work)[d, h]	Q(CDMS)[e]	Rel. diff. (%)[f]
2.725	1.000 000	5.2981(49)	5.2980	0.00	1.000 000	5.5525(50)	5.5307	0.39
5.000	1.000 000	9.4247(41)	9.4247	0.00	1.000 000	9.9416(42)	9.9014	0.40
9.375	1.000 000	17.3697(34)	17.3697	0.00	1.000 000	19.7403(36)	19.6616	0.40
18.750	1.000 000	34.4006(29)	34.4005	0.00	1.000 000	50.9055(31)	50.7102	0.38
37.500	1.000 369	68.4919(25)	68.4665	0.04	1.000 033	142.7292(30)	142.2148	0.36
75.000	1.027 795	140.402(52)	136.6050	2.70	1.007 476	405.760(45)	401.5499	1.04
150.000	1.296 184	353.73(63)	272.9036	22.85	1.130 785	1286.6(11)	1135.8099	11.72
225.000	1.842 269	753.9(21)	409.2300	45.72	1.393 281	2911.3(48)	2088.3400	28.27
300.000	2.707 133	1477.0(53)	545.5841	63.06	1.764 826	5676.3(125)	3218.5016	43.30
500.000	7.363 415	6695(31)	–	–	3.328 126	230 19.(129)	–	–

[a]The nuclear spin degeneracy is considered as 1.
[b]Result from Carvajal et al. (2019).
[c]The vibrational partition function is computed with the harmonic approximation. For more details, see the text.
[d]Q_{rv}=Q_{rot}(direct sum) Q_{vib}^{harm} unless noted otherwise. An upward estimate of the uncertainties is given in parentheses in units of the last quoted digits. For more details, see the text.
[e]Rotational partition function computed as a direct sum with no vibrational contribution. Their values are reported in CDMS catalogue (Endres et al. 2016).
[f]Relative difference of the partition function given in the present study with respect to the one reported in CDMS catalogue.
[g]The rotational contribution of the partition function is computed with a direct sum up to T = 18.75 K inclusive. From 37.50 K forward, the rotational partition function is obtained with the classical approximation. For more details, see the text.
[h]The rotational contribution of the partition function is computed with a direct sum except for T = 500 K, which is obtained with the classical approximation. For more details, see the text.

Table 3. Initial abundances assumed for the NAUTILUS model (extracted from Vidal & Wakelam (2018)). References are: 1. Wakelam & Herbst (2008); 2. Jenkins (2009); 3. Hincelin et al. (2011); 4. low-metal abundances from Graedel, Langer & Frerking (1982); 5. depleted value from Neufeld, Wolfire & Schilke (2005).

Element	n_i/n_H[a]	Ref.	Element	n_i/n_H[a]	Ref.
H_2	0.5		He	9.0(−2)	1
N	6.2(−5)	2	O	2.4(−4)	3
C^+	1.7(−4)	2	S^+	1.5(−5)	2
Fe^+	3.0(−9)	4	Si^+	8.0(−9)	4
Na^+	2.0(−9)	4	Mg^+	7.0(−9)	4
Cl^+	1.0(−9)	4	P^+	2.0(−10)	4
F	6.7(−9)	5			

[a]Abundances given in the format a(b) representing a× 10^b.

represent the HNCO abundances more accurately. Nevertheless, this approximation can furnish the first insights in the chemistry of G331. The initial elemental abundances for the core were selected from the recent values used by Vidal & Wakelam (2018) and are displayed in Table 3. They represent an intermediate-metal abundance case, in which all the abundances are the same as the low-metal one except that the amount of the element sulphur is raised to 1.5 × 10^{-5} compared with H_2 (Wakelam, Herbst & Selsis 2006). Concerning parameters such as the visual extinction, we assumed a typical value of 10 mag for a dark cloud. The gas and dust temperatures were considered the same in the simulations.

Several simulations were tested for a range of density and temperature of 10^6–10^8 cm^{-3} and 50 – 200 K, respectively (see Canelo 2020, for more details). The best-fitting model is obtained adopting a density of 1 × 10^7 cm^{-3} and a temperature of 60 K, and is presented in Fig. 8. The standard cosmic ray ionization rate for H_2 (ζ_{H_2}) is 1.3 × 10^{-17} s^{-1} (Wakelam et al. 2015; Ruaud et al. 2016), which is a key parameter for the gas-grain models since cosmic rays induce desorption processes in which chemical species pass to the gas phase from grain surfaces (Hasegawa & Herbst 1993; Ruaud et al. 2015). Taking into account that the cosmic ray ionization might vary in interstellar gas clouds, e.g. 0.6–6 × 10^{-17} s^{-1} (Van der Tak & van Dishoeck 2000; Dalgarno 2006), we also tested models considering ζ_{H_2} = 1.3 × 10^{-16} and 1.3 × 10^{-18} s^{-1}, the results are shown in Fig. 8. The main difference between the models is the plateau of the abundance intensity peaks and, consequently, the position of the maximum value. The maximum abundances obtained were 1.86, 4.19, and 5.48 × 10^{-8}, respectively. Although these abundances are a bit higher than those obtained from the rotational diagrams, the model at 60 K is the only one that can reproduce the abundance range of G331 and also the excitation temperature derived for HNCO, although the final adopted density is slightly higher than the core density derived by Hervías-Caimapo et al. (2019; see Section 1).

Downloaded from https://academic.oup.com/mnras/article/504/3/4428/6247604 by Universidad de Granada - Biblioteca user on 30 June 2021

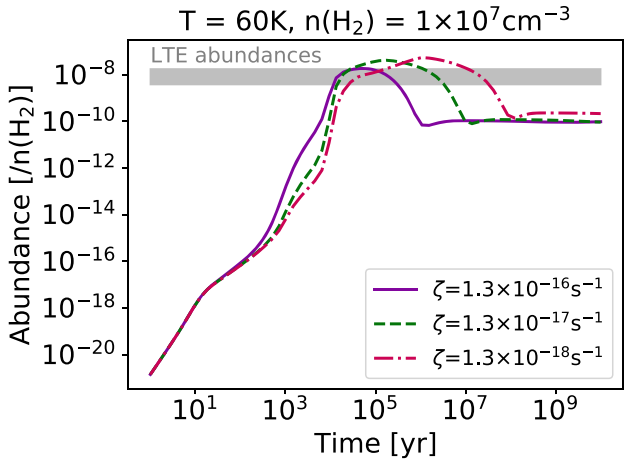

Figure 8. Best-fitting time evolution of the HNCO abundances simulated with NAUTILUS. We assumed a gas and grain temperatures of 60 K, and density of 10^7 cm^{-3}. The cosmic ray ionization rate (ζ) was varied in 1.3×10^{-16}, 1.3×10^{-17}, and 1.3×10^{-18} s^{-1}. The grey strip indicates the range of the derived LTE abundances.

From Fig. 8, it can be seen that the balance of the chemical reaction and chemical equilibrium are highly dependent on the cosmic ionization rate. Higher rates induce more chemical reactions (as expected, as it is a more significant energy source) that last a shorter period of time. Maximum abundances are also lower but the chemical equilibrium occurs faster. Considering $\zeta = 1.3 \times 10^{-17}$ s^{-1}, the chemical age could be between $3 \times 10^{4-6}$ yr with a maximum simulated abundance around 10^5 yr. The other limiting values of ζ presented the same abundance 1.4×10^{-8} derived for G331 at 10^5 yr, approximately. These models could suggest that 10^5 yr may be a plausible chemical age for G331. Hot cores and hot corinos, in general, are expected to have a dynamical age up to 10^{4-5} yr, as obtained for IRAS 16293-2422 (Hernández-Gómez et al. 2019) and G10.47+0.03 (Gorai et al. 2020), for example. Within this scenario, the chemical age derived for G331 is also in agreement with most of the objects of Fig. 7. The molecular flow of the evolved star OH231.8+4.2 has an estimated dynamical age of 800 yr, but this source is in a later evolutionary stage. Nevertheless, we cannot conclude that HNCO could be used as a chemical clock. Our simulations are zero-dimensional and this molecule can be highly dependent on the initial parameters (Hernández-Gómez et al. 2019). Moreover, the chemical age obtained with NAUTILUS is, at least, one order of magnitude larger than the estimated dynamical age of G331 (∼2000 yr, Merello et al. 2013b).

In these simulations, the code uses two formation pathways which lead to HNCO by means of gas-grain processes. The whole mechanism suggest that HNCO is initially formed on the surface of grains, via H + OCN → HNCO, then it might pass from the solid (s) to the gaseous (g) phase through sublimation processes, via HNCO (s) → HNCO (g). They are enough to reproduce the observed abundances in this temperature regime and with a zero-dimension simulation, but the code returns a greater time-scale to do it so. Furthermore, higher temperatures presented a drastic decrease in the simulated abundance. For a more robust model, with structure evolution and time evolution of physical conditions, other reactions may have to be included in the code, if their rate coefficients are available. One example is the reaction NH + CO → HNCO, normally proposed as the main pathway to form HNCO in analogous mixtures of interstellar ice processed by proton or UV radiation (Fedoseev et al. 2015). It is also possible that the incorporation of this reaction in the code may lead to a chemical age similar to the previously derived dynamical age of G331.

5 CONCLUSIONS

In this paper, we reported the observation of 42 emission lines of the potential prebiotic molecule HNCO in the hot molecular core G331. This core was observed with the *APEX* telescope covering the interval frequency 160–355 GHz. The HNCO transitions are distributed into their K_a-ladder numbers of 0, 1, and 2. The $K_a = 0$ transitions presented the highest fluxes while the $K_a = 2$ transitions showed the lowest ones, appearing as spectral pairs partially resolved. Such trends are expected from the different K_a-ladder numbers, in which the spectral pairs of each ladder get a better separation as the frequency increase. Furthermore, the observations allowed to see a particular spectral profile with extended tails in some HNCO lines, as in the HNCO $J = 8-7$ and $J = 15-14$ transitions. The HNCO emission can be responsible for about 80 per cent of the entire flux, while the wing could be an effect of the outflow or a contaminant emission.

With LTE rotational diagrams, we obtained the HNCO excitation temperature and column density of $T_{ex} = 59.4 \pm 2.3$ K and N(HNCO) $= (3.1 \pm 0.4) \times 10^{15}$ cm^{-2}, without the opacity correction, and $T_{ex} = 58.8 \pm 2.7$ K and N(HNCO) $= (3.7 \pm 0.5) \times 10^{15}$ cm^{-2}, considering beam dilution effects. This value of temperature could indicate that HNCO molecules are located in the external and colder regions of G331, according to the shell-like structure model of G331. We also derived the HNCO relative abundances by considering two main values, so that it was obtained values in the interval of $(3.8 \pm 0.5) \times 10^{-9} <$ [HNCO] $< (1.4 \pm 0.2) \times 10^{-8}$. We compared our column densities and abundances of HNCO with values from other hot molecular cores and evolved objects, and our results are in agreement with most of the objects.

In addition, the internal partition functions of the four CHNO isomers (isocyanic acid, HNCO; cyanic acid, HOCN; fulminic acid, HCNO; and isofulminic acid, HONC) have been updated with the vibrational contribution and their values are provided from 1 to 500 K in intervals of 1 K in the supplementary material. We think that this update is relevant for the estimate of abundances of the four CHNO isomers in surveys at temperatures higher than 225 K for HNCO, 150 K for HOCN, and $T = 75$ K for HCNO and HONC.

Finally, we simulated the chemistry of HNCO with the three-phase time-dependent code NAUTILUS. We used a zero-dimensional simulation with a temperature of 60 K that represented our derived abundances without the need to add more grain-phase reactions to the NAUTILUS database. We also varied the cosmic ionization rate to better comprehend the influence of this physical parameter in the simulations. From the models, we could also suggest a chemical age around 10^5 yr for G331, which is higher than estimated dynamical age. One explanation for this difference could be the absence of a key reaction to form HNCO in the code.

ACKNOWLEDGEMENTS

The authors thank the anonymous referee for the useful comments that improved the article. CMC acknowledges the support of CNPq, Conselho Nacional de Desenvolvimento Científico e Tecnológico – Brazil, process number 141714/2016-6. This study was financed in part by the Coordenação de Aperfeiçoamento de Pessoal de Nível Superior – Brasil (CAPES) – Finance Code 001. LB acknowledges support from CONICYT (Comisión Nacional de Investigación Científica

Downloaded from https://academic.oup.com/mnras/article/504/3/4428/6247604 by Universidad de Granada - Biblioteca user on 30 June 2021

y Tecnológica) project Basal AFB-170002. EM acknowledges support from the Brazilian agencies FAPESP (Fundação de Amparo à Pesquisa do Estado de São Paulo, grant 2014/22095-6) and CNPq (grant 150465/2019-0). MC acknowledges the financial support from the European Union's Horizon 2020 research and innovation program under the Marie Skłodowska-Curie grant agreement no 872081; from the Spanish National Research, Development, and Innovation plan (RDI plan) under the project PID2019-104002GB-C21; the Consejería de Conocimiento, Investigación y Universidad, Junta de Andalucía and European Regional Development Fund (ERDF), ref. SOMM17/6105/UGR; the Ministerio de Ciencia, Innovación y Universidades (ref. COOPB20364); and by the Centro de Estudios Avanzados en Física, Matemáticas y Computación (CEAFMC) of the University of Huelva.

DATA AVAILABILITY

The data underlying this article will be shared on reasonable request to the corresponding author.

REFERENCES

Albert S., Winnewisser M., Winnewisser B., 1996, Ber. Bunsenges. Phys. Chem., 100, 1876
Altwegg K. et al., 2020, Nat. Astron., 4, 533
Armstrong T., Loren R. B., 1984, Tech. Rep. AST, 8116403-1
Bally J., 2016, ARA&A, 54, 491
Belitsky V. et al., 2018, A&A, 612, A23
Bisschop S. E., Jørgensen J. K., van Dishoeck E. F., de Wachter E. B. M., 2007, A&A, 465, 913
Biver N. et al., 2006, A&A, 449, 1255
Bronfman L., Garay G., Merello M., Mardones D., May J., Brooks K. J., Nyman L.-Å., Güsten R., 2008, ApJ, 672, 391
Brunken S., Gottlieb C., McCarthy M., Thaddeus P., 2009, ApJ, 697, 880
Brünken S., Belloche A., Martín S., Verheyen L., Menten K. M., 2010, A&A, 516, A109
Canelo C. M., 2020, PhD thesis, IAG-USP, Brasil doi:https://doi.org/10.11606/T.14.2020.tde-03022021-131439
Carvajal M., Favre C., Kleiner I., Ceccarelli C., Bergin E. A., Fedele D., 2019, A&A, 627, A65
Churchwell E., Wood D., Myers P. C., Myers R. V., 1986, ApJ, 305, 405
Crovisier J., 1998, Faraday Discuss., 109, 437
Dalgarno A., 2006, Proc. Natl. Acad. Sci., 103, 12269
Dobrijevic M., Hébrard E., Loison J. C., Hickson K. M., 2014, Icarus, 228, 324
Dumke M., Mac-Auliffe F., 2010, in Proc. SPIE, Vol. 7737. p. 77371J
Duronea N. U. et al., 2019, MNRAS, 489, 1519
East A. L. L., Johnson C. S., Allen W. D., 1993, J. Chem. Phys., 98, 1299
Endres C. P., Schlemmer S., Schilke P., Stutzki J., Müller H. S. P., 2016, J. Mol. Spectrosc., 327, 95
Favre C. et al., 2014, ApJS, 215, 25
Fedoseev G., Ioppolo S., Zhao D., Lamberts T., Linnartz H., 2015, MNRAS, 446, 439
Ghesquière P., Mineva T., Talbi D., Theulé P., Noble J. A., Chiavassa T., 2015, Phys. Chem. Chem. Phys. (Inc. Faraday Trans.), 17, 11455
Goldsmith P. F., Langer W. D., 1999, ApJ, 517, 209
Gorai P., Bhat B., Sil M., Mondal S. K., Ghosh R., Chakrabarti S. K., Das A., 2020, ApJ, 895, 86
Graedel T. E., Langer W. D., Frerking M. A., 1982, ApJS, 48, 321
Greaves J. S., White G. J., 1991, A&AS, 91, 237
Güsten R., Nyman L. Å., Schilke P., Menten K., Cesarsky C., Booth R., 2006, A&A, 454, L13
Hasegawa T. I., Herbst E., 1993, MNRAS, 263, 589
He Y.-X. et al., 2021, ApJS, 253, 2
Herbst E., van Dishoeck E. F., 2009, ARA&A, 47, 427
Hernández-Gómez A., Sahnoun E., Caux E., Wiesenfeld L., Loinard L., Bottinelli S., Hammami K., Menten K. M., 2019, MNRAS, 483, 2014
Hervías-Caimapo C. et al., 2019, ApJ, 872, 200
Herzberg G., 1991, Spectra and Molecular Structure: II. Infrared and Raman Spectra of Polyatomic Molecules. Krieger Pub. Co., Malabar, Florida
Hincelin U., Wakelam V., Hersant F., Guilloteau S., Loison J. C., Honvault P., Troe J., 2011, A&A, 530, A61
Hocking W. H., Gerry M. C. L., Winnewisser G., 1972, ApJ, 174, L93
Hocking W. H., Gerry M. C. L., Winnewisser G., 1974, ApJ, 187, L89
Hocking W. H., Gerry M. C. L., Winnewisser G., 1975, Can. J. Phys., 53, 1869
Jenkins E. B., 2009, ApJ, 700, 1299
Jensen P., 1983, J. Mol. Spectrosc., 101, 422
Jewell P. R., Hollis J. M., Lovas F. J., Snyder L. E., 1989, ApJS, 70, 833
Jones L. H., Badger R. M., 1950, J. Chem. Phys., 18, 1511
Jones L. H., Shoolery J. N., Shulman R. G., Yost D. M., 1950, J. Chem. Phys., 18, 990
Khalouf-Rivera J., Pérez-Bernal F., Carvajal M., 2020, J. Quant. Spectrosc. Radiat. Transfer, 261, 107436
Lapinov A. V., Golubiatnikov G. Y., Markov V. N., Guarnieri A., 2007, Astron. Lett., 33, 121
Li J., Wang J. Z., Gu Q. S., Zheng X. W., 2013, A&A, 555, A18
Ligterink N. F. W., Terwisscha van Scheltinga J., Taquet V., Jørgensen J. K., Cazaux S., van Dishoeck E. F., Linnartz H., 2018, MNRAS, 480, 3628
Lis D. C. et al., 1997, Icarus, 130, 355
López-Sepulcre A. et al., 2015, MNRAS, 449, 2438
López-Sepulcre A., Balucani N., Ceccarelli C., Codella C., Dulieu F., Theulé P., 2019, ACS Earth Space Chem., 3, 2122
Loren R. B., Mundy L. G., 1984, ApJ, 286, 232
Lovas F. J., 2004, J. Phys. Chem. Ref. Data, 33, 177
MacDonald G. H., Gibb A. G., Habing R. J., Millar T. J., 1996, A&AS, 119, 333
Marcelino N., Cernicharo J., Tercero B., Roueff E., 2009, ApJ, 690, L27
Martín S., Mauersberger R., Martín-Pintado J., Henkel C., García-Burillo S., 2006, ApJS, 164, 450
Martín S., Requena-Torres M. A., Martín-Pintado J., Mauersberger R., 2008, ApJ, 678, 245
Martín S., Martín-Pintado J., Mauersberger R., 2009, ApJ, 694, 610
Martín-Doménech R., Rivilla V. M., Jiménez-Serra I., Quénard D., Testi L., Martín-Pintado J., 2017, MNRAS, 469, 2230
McLean A., Loew G., Berkowitz D., 1977, J. Mol. Spectrosc., 64, 184
Meier D. S., Turner J. L., 2005, ApJ, 618, 259
Mendoza E., Lefloch B., López-Sepulcre A., Ceccarelli C., Codella C., Boechat-Roberty H. M., Bachiller R., 2014, MNRAS, 445, 151
Mendoza E. et al., 2018, ApJ, 853, 152
Merello M., Bronfman L., Garay G., Nyman L.-Å., Evans, Neal J. I., Walmsley C. M., 2013a, ApJ, 774, 38
Merello M., Bronfman L., Garay G., Lo N., Evans N. J. II, Nyman L. Å., Cortés J. R., Cunningham M. R., 2013b, ApJ, 774, L7
Mladenovic M., Lewerenz M., 2008, Chem. Phys., 343, 129
Mladenovic M., Lewerenz M., McCarthy M., Thaddeus P., 2009, J. Chem. Phys., 131, 174308
Neufeld D. A., Wolfire M. G., Schilke P., 2005, ApJ, 628, 260
Nguyen-Q-Rieu, Henkel C., Jackson J. M., Mauersberger R., 1991, A&A, 241, L33
Niedenhoff M., Yamada K. M. T., Belov S. P., Winnewisser G., 1995, J. Mol. Spectrosc., 174, 151
Nummelin A., Bergman P., Hjalmarson Å., Friberg P., Irvine W. M., Millar T. J., Ohishi M., Saito S., 1998, ApJS, 117, 427
Pickett H. M., 1991, J. Mol. Spectrosc., 148, 371
Pickett H. M., Poynter R. L., Cohen E. A., Delitsky M. L., Pearson J. C., Müller H. S. P., 1998, J. Quant. Spectrosc. Radiat. Transfer, 60, 883
Prasad S. S., Tarafdar S. P., 1983, ApJ, 267, 603
Reboussin L., Wakelam V., Guilloteau S., Hersant F., 2014, MNRAS, 440, 3557
Ruaud M., Loison J. C., Hickson K. M., Gratier P., Hersant F., Wakelam V., 2015, MNRAS, 447, 4004
Ruaud M., Wakelam V., Hersant F., 2016, MNRAS, 459, 3756

Downloaded from https://academic.oup.com/mnras/article/504/3/4428/6247604 by Universidad de Granada - Biblioteca user on 30 June 2021

Schulze G., Koja O., Winnewisser B., Winnewisser M., 2000, J. Mol. Struct., 517/518, 307
Semenov D. et al., 2010, A&A, 522, A42
Shimanouchi T., 2018, Molecular Vibrational Frequencies in NIST Chemistry WebBook. NIST Standard Reference Database Number 69. P.J. Linstrom and W.G. Mallard, National Institute of Standards and Technology, Gaithersburg MD, 20899, USA
Snyder L. E., Buhl D., 1972, ApJ, 177, 619
Snyder L. E. et al., 2005, ApJ, 619, 914
Su H., Kong F., Chen B., Huang M., Liu Y., 2000, J. Chem. Phys., 113, 1885
Sutton E. C., Blake G. A., Masson C. R., Phillips T. G., 1985, ApJS, 58, 341
Sutton E. C., Jaminet P. A., Danchi W. C., Blake G. A., 1991, ApJS, 77, 255
Takashi R., Tanaka K., Tanaka T., 1989, J. Mol. Spectrosc., 138, 450
Turner B. E., 1991, ApJS, 76, 617
Van der Tak F. F. S., van Dishoeck E. F., 2000, A&A, 358, L79
Vassilev V. et al., 2008, A&A, 490, 1157
Velilla Prieto L. et al., 2015, A&A, 575, A84
Vidal T. H. G., Wakelam V., 2018, MNRAS, 474, 5575
Wakelam V., Herbst E., 2008, ApJ, 680, 371
Wakelam V., Herbst E., Selsis F., 2006, A&A, 451, 551
Wakelam V. et al., 2015, ApJS, 217, 20
Wells T., Raston P., 2020, J. Mol. Spectrosc., 370, 111292
Winnewisser M., Winnewisser B., 1971, Z. Naturforsch., 26, 128
Wyrowski F., Schilke P., Walmsley C. M., 1999, A&A, 341, 882
Zinchenko I., Henkel C., Mao R. Q., 2000, A&A, 361, 1079

APPENDIX A: CALCULATION OF THE PARTITION FUNCTIONS OF CHNO ISOMERS

Here we are giving some details for the calculation of the rovibrational partition function for the isomers of CHNO isomers (isocyanic acid, cyanic acid, fulminic acid, and isofulminic acid).

A1 Isocyanic acid (HNCO)

Isocyanic acid is a near-prolate asymmetric top of which rotational-vibrational partition function has been previously calculated (Carvajal et al. 2019). The main results of this isomer have been included here to compare them with the internal partition functions of the other three isomers. Thus, here we only outline the details for its calculation.

The internal partition function has been computed from equation (4). The rotational partition function has been computed as a direct sum taking into consideration the rotational energies predicted up to $J = 135$ and $K_a = 30$ from the Hamiltonian provided by Lapinov et al. (2007). The harmonic vibrational partition function has been calculated with the experimental vibrational fundamental frequencies recorded by East, Johnson & Allen (1993).

A2 Cyanic acid (HOCN)

Cyanic acid is a bent molecule with a near-prolate asymmetric top structure of which rotational spectrum has been measured in the centimetre- and millimetre-wave windows (Brunken et al. 2009). This molecular species has no available experimental vibrational energies in the gas phase except the ν_2 band (Su et al. 2000; Shimanouchi 2018) but the complete set of fundamental frequencies have been obtained theoretically (Mladenovic & Lewerenz 2008).

The values of the rotational partition function calculated as a direct sum and as a classical approximation are given in Table A1. The direct sum is obtained using the predicted rotational energy levels up to $J = 72$ and $K_a = 8$ (Brunken et al. 2009) provided in the CDMS (Endres et al. 2016). The classical approximation is computed with the rotational constants from Brunken et al. (2009). In Table A1, it can be observed that the relative differences between the two procedures are relatively small for temperatures above T = 18.75 K. Nevertheless, it should be highlighted that, for temperatures from 37.5 to 300 K, the direct sum results in slightly smaller values than the ones provided by the classical approximation. This fact could suggest that the direct sum has not been converged for this temperature interval. On the contrary, the direct sum has reached the convergence because, if this had not been reached at T = 37.5 K, the difference between the direct sum and the classical approximation would have been increased for higher temperatures. In addition, we have compared the values obtained through the direct sum in this work and the rotational partition function values provided in the CDMS (Endres et al. 2016), which are also reported in Table 2. It can be observed that the values of the direct sum in this work and those from CDMS, which only provides values up to T = 300 K, are practically the same. The relative difference between them is smaller than 0.00 per cent except for T = 300 K, which is of −0.04 per cent. Thus, it can be considered that the direct sum values of the rotational partition function have reached the convergence for all the temperature range up to T = 300 K. However, at 500 K, according to the increasing difference between the direct sum and the classical approximation, we can state that the direct sum has not converged for this temperature. Therefore, even though the convergence of the direct sum seems to be reached up to T = 300 K, we will consider for the rotational partition function in equation (4) the values of the direct sum up to T = 36 K inclusive and of the classical approximation from T = 37 K up, according to the highest value.

Table A1. Rotational partition function for cyanic acid (HOCN). Comparison between the direct sum values and the classical approximation[a].

	HOCN		
T(K)	$Q_{\rm rot}^{\rm approx}$ [b]	$Q_{\rm rot}$ (direct sum)[c]	Rel. Diff. (per cent)[d]
2.725	2.78	5.76	51.66
5.000	6.92	10.30	32.83
9.375	17.77	20.12	11.70
18.750	50.26	50.82	1.09
37.500	142.16	142.14	−0.01
75.000	402.08	401.38	−0.18
150.000	1137.25	1135.36	−0.17
225.000	2089.27	2087.44	−0.09
300.000	3216.64	3215.89	−0.02
500.000	6921.10	6863.28	−0.84

[a]Nuclear spin degeneracy is considered as 1.
[b]Rotational partition function computed with the classical approximation using the rotational constants from Brunken et al. (2009).
[c]Rotational partition function computed as a direct sum considering the predicted rotational energy levels up to $J = 72$ and $K_a = 8$ (Brunken et al. 2009). The predicted rotational energies are also given in CDMS (Endres et al. 2016).
[d]Relative differences.

The vibrational partition function has been obtained using the harmonic approximation from the *ab initio* fundamental vibrational frequencies calculated with the CCSD(T)/cc-pVQZ(all) level of theory (Mladenovic & Lewerenz 2008). Their values are given in Table 2 together with the values of rovibrational partition function computed with equation (4) as well as those up to 300 K of the CDMS rotational partition function. The relative difference between

Downloaded from https://academic.oup.com/mnras/article/504/3/4428/6247604 by Universidad de Granada - Biblioteca user on 30 June 2021

Table A2. Rotational partition function for fulminic acid (HCNO). Comparison between the direct sum values and the classical approximation[a].

		HCNO	
T(K)	$Q_{rot}^{approx\ b}$	Q_{rot} (directsum)[c]	Rel. diff. (per cent)[d]
2.725	4.950 696	5.298 078	6.56
5.000	9.083 845	9.424 730	3.62
9.375	17.032 210	17.369 697	1.94
18.750	34.064 420	34.400 567	0.98
37.500	68.128 841	68.466 594	0.49
75.000	136.257 682	136.605 301	0.25
150.000	272.515 363	272.904 169	0.14
225.000	408.773 045	409.230 843	0.11
300.000	545.030 726	545.585 087	0.10
500.000	908.384 544	909.229 250	0.09

[a]Nuclear spin degeneracy is considered as 1.
[b]Rotational partition function computed with the classical approximation for linear molecules using the rotational constant from Winnewisser & Winnewisser (1971).
[c]Rotational partition function computed as a direct sum considering the predicted rotational energy levels up to $J = 90$ (Winnewisser & Winnewisser 1971). The predicted rotational energies are also reported in the CDMS (Endres et al. 2016).
[d]Relative differences.

Table A3. Rotational partition function for isofulminic acid (HONC). Comparison between the direct sum values and the classical approximation[a].

		HONC	
T(K)	$Q_{rot}^{approx\ b}$	Q_{rot} (directsum)[c]	Rel. diff. (per cent)[d]
2.725	2.782 829	5.552 537	49.88
5.000	6.916 585	9.941 600	30.43
9.375	17.757 982	19.740 254	10.04
18.750	50.227 159	50.905 466	1.33
37.500	142.063 859	142.724 545	0.46
75.000	401.817 274	402.748 482	0.23
150.000	1136.510 876	1137.826 802	0.12
225.000	2087.903 800	2089.514 569	0.08
300.000	3214.538 189	3216.363 948	0.06
500.000	6916.584 928	6911.736 014	− 0.07

[a]Nuclear spin degeneracy is considered as 1.
[b]Rotational partition function computed with the classical approximation using the rotational constants from Mladenovic et al. (2009).
[c]Rotational partition function computed as a direct sum considering the predicted rotational energy levels up to $J = 80$ calculated through SPCAT code (Pickett 1991) using the rotational parameters from Mladenovic et al. (2009).
[d]Relative differences.

the results of this work and of CDMS become larger than 10 per cent at 225 K of temperature. Despite it is expected that the new values of the internal partition function are more precise, a more comprehensive list of experimental and predicted rovibrational data would be necessary to improve the partition function values as well as to get the convergence for the direct sum along all the interval up to T = 500 K.

In the supplementary material, it is provided the rotational (as a direct sum up to T = 36 K and from this temperature forward as a classical approximation), vibrational and rovibrational partition function computed in the present work for cyanic acid (HOCN) up to T = 500 K using a 1 K interval.

A3 Fulminic acid (HCNO)

Fulminic acid is a linear molecule of which experimental spectrum has been recorded in the millimetre-wave rotational and infrared ranges (Winnewisser & Winnewisser 1971; Albert, Winnewisser & Winnewisser 1996; Schulze et al. 2000). The internal partition function has been computed using equation (4) where the rotational partition function has been calculated as a direct sum and compared in Table A2 to the classical approximation for a linear molecule (Herzberg 1991).

The direct sum of the rotational partition function has been obtained considering the predicted rotational energies in the vibrational ground state up to $J = 90$. The predictions have been calculated from the rotational Hamiltonian provided by Winnewisser & Winnewisser (1971) although, in this particular case, they have also been reported in the CDMS (Endres et al. 2016). The classical approximation has been calculated from the rotational constant B provided by Winnewisser & Winnewisser (1971). In Table A2, it can be observed that the classical approximation has a good agreement with the direct sum from T = 18.75 K up and, although slightly smaller, the difference decreases for higher temperatures.

The harmonic approximation of the vibrational partition function has been obtained using the experimental fundamental vibrational energies (Albert et al. 1996; Schulze et al. 2000; Shimanouchi 2018). These values are given in Table 2 together with the values of the internal partition function, written as product of the direct sum of the rotational contribution and harmonic approximation of the vibrational contribution, and the CDMS rotational partition function calculated as a direct sum (Endres et al. 2016). In addition, the relative difference between the internal partition function obtained in this work and the CDMS partition function is also given. It can be noted that the relative difference is larger than 20 per cent at temperatures higher than 150 K. CDMS does not provide the partition function at T = 500 K.

In the supplementary material, it is reported the rotational (as a direct sum), vibrational, and rovibrational partition function computed in the present work for fulminic acid (HCNO) up to T = 500 K using a 1 K interval.

A4 Isofulminic acid (HONC)

Isofulminic acid is the CHNO isomer with less spectroscopic information. This molecule is a non-linear asymmetric top molecule close to the prolate limit. Up to the present, the only experimental spectroscopic paper about this species provides some microwave data as well as *ab initio* calculations of the rotational parameters and the fundamental vibrational energies (Mladenovic et al. 2009).

Despite the lack of data, the rotational partition function has been calculated as a direct sum and this has been compared to the values given by the classical approximation (see Table A3). The direct sum has been calculated from the rotational energies up to $J = 80$ and $K_a = 20$ predicted with SPCAT code (Pickett 1991) using the experimental value of the rotational constant B and the *ab initio* values of the rotational constants A and C (Mladenovic et al. 2009). These latter parameters have also been used for the classical approximation. The comparison between the direct sum and the classical approximation for the rotational partition function is also provided in Table A3. From temperatures above 18.75 K, the relative difference is rather small and decreases for higher temperatures. Nevertheless, it can be noted that the value of the

Downloaded from https://academic.oup.com/mnras/article/504/3/4428/6247604 by Universidad de Granada - Biblioteca user on 30 June 2021

classical approximation becomes slightly larger (with a relative difference smaller than 0.1 per cent) than the direct sum at T = 500 K. This reveals that, at any temperature above, when this difference will become substantially larger, the convergence of the direct sum obtained with the present spectroscopic data will not be reached anymore.

The values of the harmonic approximation of the vibrational partition function are given in Table 2 together with the rovibrational ones calculated through equation (4). The vibrational partition function is worked out using the fundamental vibrational frequencies determined with the *ab initio* CCSD(T)/cc-pCVTZ level of theory (Mladenovic et al. 2009). To calculate the rovibrational partition function, the values of the rotational direct sum are considered up to T = 437 K inclusive since the direct sum provides larger values than those of the classical approximation. Above this temperature, the classical approximation is considered in its stead. In addition, in Table 2, the internal partition function of this work is set side by side with the values of the rotational partition function reported in the CDMS up to T = 300 K (Endres et al. 2016). It should be highlighted that the relative difference is larger than 10 per cent at the temperature of 150 K. In any way, a more precise partition function could be determined in case that new experimental spectral measurements as well as experimental fundamentals are available.

In the supplementary material, it is reported the rotational (as a direct sum up to T = 437 K and from this temperature on as a classical approximation), vibrational, and rovibrational partition function computed in the present work for isofulminic acid (HONC) up to T = 500 K using a 1 K interval.

This paper has been typeset from a TEX/LATEX file prepared by the author.

Downloaded from https://academic.oup.com/mnras/article/504/3/4428/6247604 by Universidad de Granada - Biblioteca user on 30 June 2021